Inorganic Chemistry

pubs.acs.org/IC Article

Insights into Molecular Magnetism in Metal−Metal Bonded Systems as Revealed by a Spectroscopic and Computational Analysis of Diiron Complexes

Samuel M. Greer, Kathryn M. Gramigna, Christine M. Thomas,* Sebastian A. Stoian,* and Stephen Hill*

Cite This: *Inorg. Chem.* 2020, 59, 18141−18155 Read Online

ACCESS | Metrics & More | Article Recommendations | Supporting Information

ABSTRACT: A pair of bimetallic compounds featuring Fe−Fe bonds, [Fe(^{i}PrNPPh$_2$)$_3$FeR] (R = PMe$_3$, ≡N^{t}Bu), have been investigated using High-Frequency Electron Paramagnetic Resonance (HFEPR) as well as field- and temperature-dependent ^{57}Fe nuclear γ resonance (Mössbauer) spectroscopy. To gain insight into the local site electronic structure, we have concurrently studied a compound containing a single Fe(II) in a geometry analogous to that of one of the dimer sites. Our spectroscopic studies have allowed for the assessment of the electronic structure via the determination of the zero-field splitting and ^{57}Fe hyperfine parameters for the entire series. We also report on our efforts to correlate structure with physical properties in metal−metal bonded systems using ligand field theory guided by quantum chemical calculations. Through the insight gained in this study, we discuss strategies for the design of single-molecule magnets based on polymetallic compounds linked via direct metal−metal bonds.

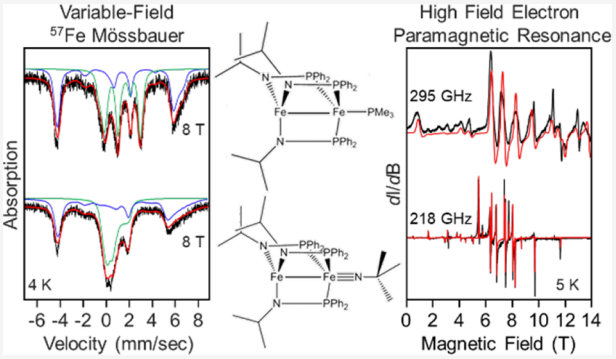

INTRODUCTION

Tuning magnetic interactions between multiple spin-carrying metals to elicit the desired magnetic/electronic properties has long been a goal in molecular magnetism research.[1] Of particular interest is the tunability of the zero-field splitting (ZFS) parameters, which, when properly adjusted, provide a barrier to the reversal of magnetization in single-molecule magnets (SMMs).[2] A great deal of this work has focused on exchange-coupled clusters where the interaction between magnetic ions is mediated by a (usually) diamagnetic bridging group.[3−5] While these superexchange interactions can generate a large ground state spin, they are usually weak and lead to a poorly isolated ground state.[6] In these cases, the ZFS is often similar in energy to the separation between ground and excited spin multiplets and, thus, can allow for significant mixing of ground and excited spin states.[7−11] This mixing provides undesirable relaxation pathways that permit the quantum tunneling of magnetization.[12−15] Recently, SMM behavior has been observed in clusters featuring covalent bonds between metal sites.[16] In dimers of transition metals, strong bonding interactions and high-spin ground states are antagonistic to one another, i.e., bonds between metals tend to result in low spin states.[17] This is due to the large separation between bonding and antibonding orbitals induced by strong metal−metal interactions. The overall spin state is then a function of both the orbital separation and the electron pairing energy. In the strong-interaction regime, the separation induced by orbital interactions is larger than the pairing energy and therefore results in a low spin state. A relatively small number of examples have been reported where two metals, joined by a single covalent bond, exhibit ground states with large spins.[18−25] To investigate this unique class of high-spin metal−metal-bonded systems, we have studied a pair of compounds where the diiron bond is supported by an ambidentate phosphinoamide ligand as well as a monoiron analogue where the tris-amide site is occupied by a high-spin Fe(II), **1**. The bimetallic compounds have the general formula [Fe(^{i}PrNPPh$_2$)$_3$FeR], where R = PMe$_3$ (**2**), ≡N^{t}Bu (**3**). In both zwitterionic complexes, absent the metal−metal bond, the tris(amide) coordinated site is expected to be formally Fe(II) while the tris(phosphine) site is formally Fe(I) and Fe(III) in **2** and **3**, respectively (Figure 1). To probe the electronic structures of **1**−**3**, we have performed detailed high-frequency electron paramagnetic resonance (HFEPR) and ^{57}Fe nuclear γ

Received: September 1, 2020
Published: November 30, 2020

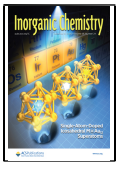

https://dx.doi.org/10.1021/acs.inorgchem.0c02605
Inorg. Chem. 2020, 59, 18141−18155

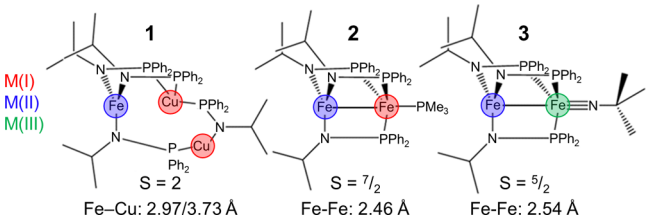

Figure 1. Schematic structures of the compounds investigated in this report along with experimentally established spin states and crystallographic Fe–Fe distances or, in the case of **1**, Fe–Cu distances. The color highlighting each metal ion is indicative of the formal oxidation state of each site absent any metal–metal bonding interactions: red (+1), blue (+2), and green (+3).

resonance (Mössbauer) spectroscopy measurements. We have rationalized the observed spectroscopic parameters in terms of ligand field theory guided by quantum chemical calculations.

MATERIALS AND METHODS

Synthesis. The compounds studied in this report are both air and moisture sensitive. Therefore, all sample preparations were carried out in an inert-atmosphere glovebox and all additional manipulations were performed while the samples were kept under liquid nitrogen at 77 K. All compounds were synthesized as previously reported.[19,26]

^{57}Fe Nuclear γ Resonance or Mössbauer Spectroscopy. The samples contained ∼50 mg of polycrystalline material constrained with mineral oil in a polyethylene cup. The Mössbauer spectra were collected using a Janis cryostat fitted with a built-in superconducting magnet capable of producing magnetic fields with a maximum strength of 8 T. The field was applied parallel to the propagation direction of the 14.4 keV γ rays used to detect the Mössbauer effect. This spectrometer was used to record spectra at temperatures ranging from 4.2 to 250 K. The isomer shift is reported relative to that of α-Fe at room temperature. All simulated spectra were computed using the WMOSS software package.[27]

High-Frequency Electron Paramagnetic Resonance (HFEPR). Spectra were collected on microcrystalline, neat powder samples that were immobilized in a polyethylene cup capped with a Teflon stopper. The transmission-type spectrometer used in this study employed a 17 T superconducting magnet (Oxford Instruments Ltd., Abingdon, U.K.).[28] Microwaves of selected frequencies were generated using a phase-locked source (Virginia Diodes Inc., Charlottesville, VA) combined with a series of frequency multipliers. Detection of the field-modulated signal was achieved using a hot electron InSb bolometer (QMC Instruments Ltd., Cardiff, U.K.). Temperature control was achieved using a variable-flow helium cryostat (Oxford Instruments Ltd., Abingdon, U.K.). Spectral simulations were generated using EasySpin.[29] All samples were investigated by zero-field Mössbauer spectroscopy before and after the HFEPR experiments to ensure that both measurements were performed for the same chemical species.

Calculations. Density functional theory (DFT) calculations of electric field gradients (EFG), isomer shifts, and hyperfine coupling $\tilde{\mathbf{A}}$ tensors were performed using unoptimized structural models derived from the reported structures determined by single-crystal X-ray diffraction measurements.[19,26] Calculations were performed using the BP86/CP(PPP)(Fe), def2-tzvp(P/N), and def2-svp(C/H) functional/basis set combinations in conjunction with the resolution of the identity approximation and auxiliary basis sets generated using the "autoaux" command.[30−33] The calculated electron densities at the Fe nuclei were converted into isomer shift values using the calibration reported by Römelt et al.[34] This functional choice has previously proven successful in modeling the structure, spin state energetics, EFG, isomer shift, and hyperfine interactions in metal–metal-bonded systems.[35,36] For comparison, the results for **1** obtained using the more popular B3LYP functional are also presented in the Supporting Information. For these calculations the spin–orbit coupling operator was computed using the mean-field approximation (SOMF).[37] To facilitate complete active space self-consistent field (CASSCF) calculations, truncated structural models were generated from the experimental crystal structures by converting all P- and N-bound R groups into CH_3. A constrained-geometry optimization of these models was performed where only the C/H positions were optimized. This procedure allowed for the preservation of the crystallographically determined Fe–Fe core. The active space of **1** consisted of the 5 Fe-based 3d orbitals and 6 d electrons. The state averaged CASSCF (SA-CASSCF) calculation for **1** used the minimum active space of 6 electrons in the 5 3d orbitals and included all 5 quintet states and all 45 triplet states. The active space of **2** was spanned by the 10 3d orbitals (5 from each Fe) and 13 electrons. This electron count was selected on the basis of the fact that the tris(amide)-coordinated metal site of **2** is expected to be formally Fe(II) and, thus, to have 6 d electrons, while the tris(phosphine) site is formally Fe(I) and contributes 7 electrons, yielding a total of 13 d electrons in the active space. This calculation was performed twice; the first considered 10 roots each for both octet and sextet multiplicities, and the second calculated 30 roots for each. The SA-CASSCF calculations for **3** used

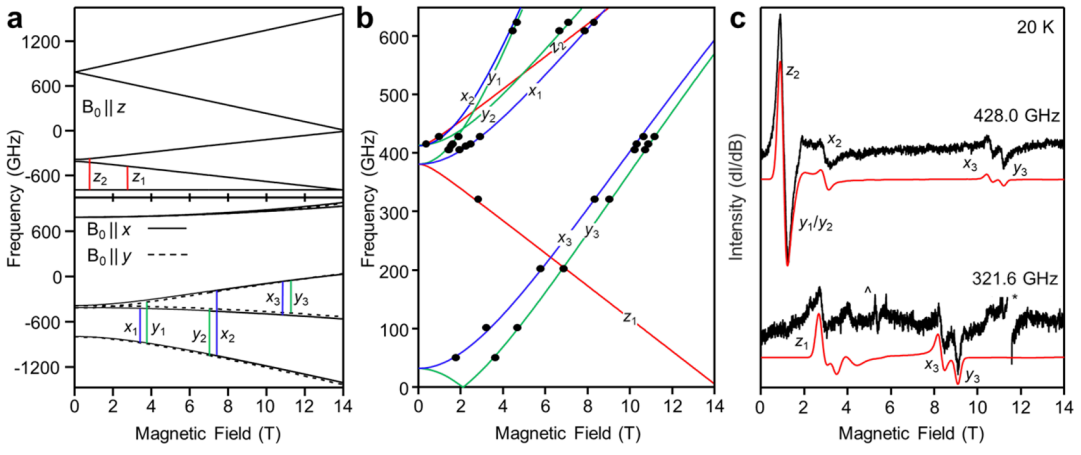

Figure 2. (a) Energy levels of the ground quintet state as a function of applied magnetic field for the three principal axes of the ZFS tensor of **1**. The vertical lines indicate observed resonances. (b) Two-dimensional frequency vs resonant field plot showing the observed EPR transitions. Black circles represent the experimentally observed resonance positions. Curves were calculated with the field applied along the principal components of the ZFS tensor: x (blue), y (green), and z (red). Only curves corresponding to observed transitions are shown. The same color scheme is used to indicate transitions in (a). (c) Representative experimental EPR spectra (black) and simulations (red).

https://dx.doi.org/10.1021/acs.inorgchem.0c02605
Inorg. Chem. 2020, 59, 18141−18155

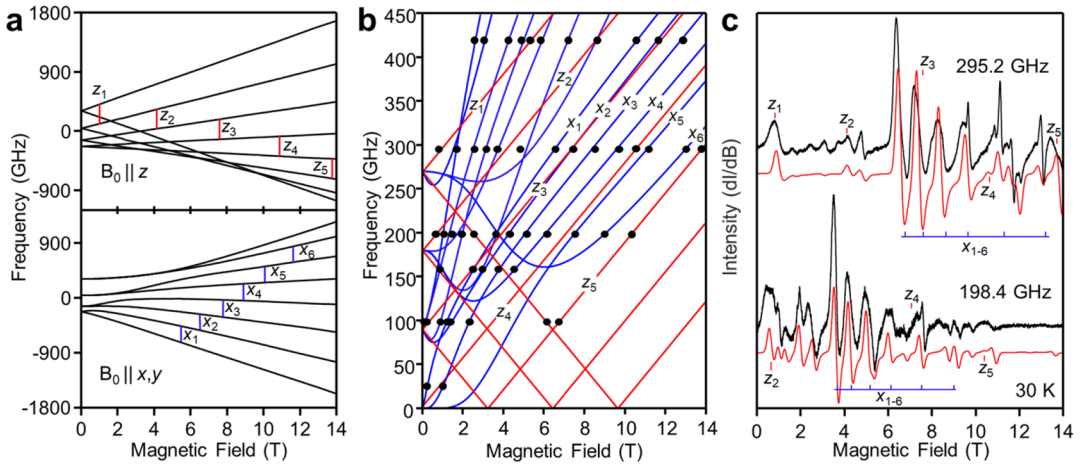

Figure 3. (a) Energy levels of the ground octet state as a function of applied magnetic field for the three principal axes of the ZFS tensor of **2**. The vertical lines indicate observed resonances. (b) Two-dimensional frequency vs resonant field plot showing the observed EPR transitions. Black circles represent the experimentally observed resonance positions. Curves were calculated with the field applied along the principal components of the ZFS tensor: *x*/*y* (blue) and *z* (red). The same color scheme is used to indicate transitions in (a). Only curves corresponding to observed transitions are shown. (c) Representative experimental EPR spectra (black) and simulations (red).

an expanded active space consisting of 12 orbitals and 15 electrons, considering 40 sextet, 20 quartet, and 20 octet states. In this case, the 2 nitrogen-based p orbitals involved in the Fe−N π bond were also included beyond the 10 canonical metal-based 3d orbitals. The 15 electrons in the active space originate from the tris(amide)-coordinated Fe site, formally a Fe(II) ion with a d^6 electronic configuration, and the tris(phosphine) Fe site, which formally is a Fe(III) ion with a d^5 configuration. Four additional electrons originated from 2 Fe−N π-bonding orbitals each populated by 2 electrons. In all CASSCF calculations scalar relativistic effects were accounted for by the second-order Douglas−Kroll−Hess (DKH) procedure.[38−41] The converged wave functions were then subjected to *N*-electron valence perturbation theory to second order (NEVPT2) to account for dynamic correlation.[42−45] All calculations were performed using the Orca 4.0 program package.[46]

RESULTS

High Frequency Electron Paramagnetic Resonance. Multifrequency EPR was utilized in order to directly quantify the ZFS parameters and *g* factors of **1**−**3**. The EPR spectra were analyzed in the framework of a standard spin Hamiltonian

$$\hat{H}_{\text{elec}} = \beta_e \vec{\mathbf{B}}\cdot\tilde{\mathbf{g}}\cdot\hat{\mathbf{S}} + D\left[\hat{S}_z^2 - \frac{S(S+1)}{3} + \frac{E}{D}(\hat{S}_x^2 - \hat{S}_y^2)\right] \quad (1)$$

where β_e is the Bohr magneton, $\vec{\mathbf{B}}$ is the applied magnetic field vector, $\tilde{\mathbf{g}}$ is the Landé tensor, D/E are the axial and rhombic ZFS parameters, $\hat{\mathbf{S}}$ is the total electronic spin operator, and $\hat{S}_\mu$ ($\mu = x, y, z$) is its components.

HFEPR Spectra of ***1***. The metallic core of **1** consists of one formal Fe(II) ion and two Cu(I) ions. Both Cu(I) ions have a d^{10} electronic configuration and, therefore, are diamagnetic. The Fe(II) site exhibits a high-spin state, resulting in an overall spin of $S = 2$ (Figure 2a). For **1**, the observed resonance positions were gathered into a 2D frequency versus resonant field plot, which is shown in Figure 2b. The spin Hamiltonian parameters of the ground quintet state were extracted by examining a few key regions of Figure 2b: (i) the low-field/low-frequency behavior of the resonances associated with the x_3/y_3 branches and (ii) the pair of branches that emerge at ∼400 GHz, labeled x_2/y_2 and x_1/y_1. In an axial system ($E = 0$) with $D > 0$ (*vide infra*) the ground state is a singlet with $M_S = 0$, while the first excited states are the doubly degenerate $M_S = \pm 1$ levels. When the symmetry of the system is lowered ($E \neq 0$), the degeneracy of the $M_S = \pm 1$ states will lift, establishing a zero-field energy gap with a magnitude equal to $6E$. This splitting allows for an additional transition between the $M_S = \pm 1$ states. Tracing the frequency-dependent behavior of the x_3-branch to zero field reveals an energy gap of ∼32 GHz, which allows for a direct measure of *E*. To determine *D* and acquire an additional measurement of *E*, the high-frequency spectra must also be examined. In the axial limit, a single transition from $M_S = 0 \rightarrow \pm 1$ is expected to emerge at the frequency equal to the zero-field splitting of these spin sublevels. However, due to the nonzero *E* value in **1**, we expect two emergent branches centered at *D* and split by $6E$, which is known to be ∼32 GHz from the zero-field intercept of the x_3/y_3 transitions. Indeed, we observe two groups of transitions, x_1/y_1 and x_2/y_2, which can be extrapolated to two different zero-field intercepts centered at ∼397 GHz and split by ∼32 GHz. From these observations, we determine that $|D| = 13.24$ cm^{-1} and $|E| = 0.18$ cm^{-1} ($E/D = 0.014$), respectively. To ascertain the sign of *D*, spectra were recorded at several temperatures, which show that the relative intensities of x_1/y_1 and x_2/y_2 decrease, while those of the x_3/y_3 transitions increase. This behavior demonstrates a positive *D*, which was further confirmed by subsequent spectral simulations (Figure 2c). With the ZFS parameters known, the *g* values were determined by reproducing the frequency dependence of the resonance positions. By following the transitions to higher fields, the individual components of the $\tilde{\mathbf{g}}$ tensor were found to be $g_x = 2.24$, $g_y = 2.25$, and $g_z = 2.00$. This parameter set reproduces both the individual spectra as well as the global frequency dependence, as shown in Figure 2b,c. We note that, since the ZFS is directly observed, the constraints on the spin Hamiltonian parameters are very strong.

HFEPR Spectra of ***2***. In the absence of the metal−metal bond, the formal oxidation states of the two Fe sites of **2** are assigned as +1 (tris(phosphine) site) and +2 (tris(amide) site) with d^7 and d^6 electronic configurations, respectively. Therefore, there are a total of 13 3d electrons in 10 d-based orbitals. The highest possible spin that can be achieved for this electron

https://dx.doi.org/10.1021/acs.inorgchem.0c02605
Inorg. Chem. 2020, 59, 18141−18155

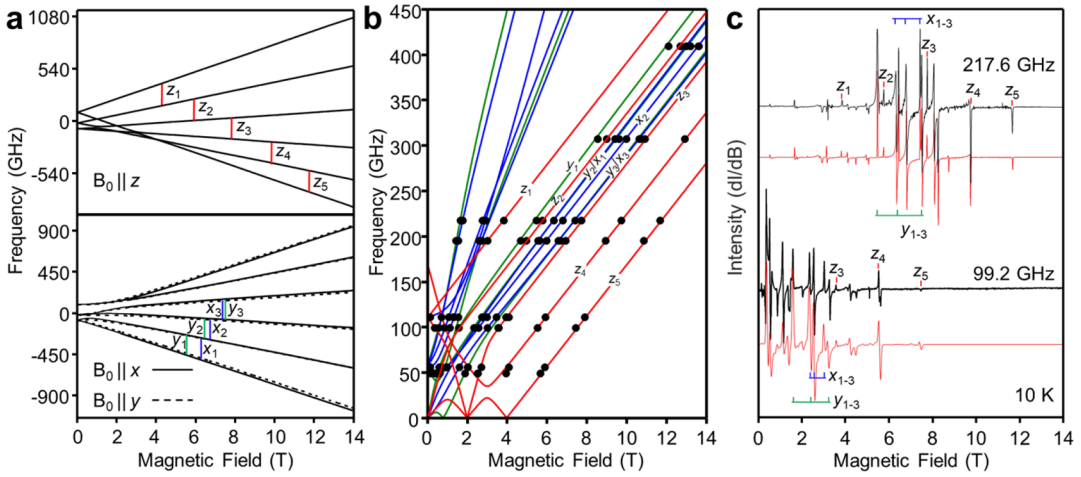

Figure 4. (a) Energy levels of the ground sextet state as a function of applied magnetic field for the three principal axes of the ZFS tensor of **3**. The vertical lines indicate observed resonances. (b) Two-dimensional frequency vs resonant field plot showing the observed EPR transitions. Black circles represent the experimentally observed resonance positions. Curves were calculated with the field applied along the principal components of the ZFS tensor: *x*/*y* (blue/green) and *z* (red). Only curves corresponding to observed transitions are shown. (c) Representative experimental EPR spectra (black) and simulations (red).

count is $S = 7/2$. Previous magnetic susceptibility measurements for **2** were consistent with a ground octet state and, thus, we analyzed the spectra using eq 1 with $S = 7/2$ (Figure 3a). The 4 K HFEPR spectra of **2** are dominated by numerous features that coalesce at elevated temperatures (Figure S1). This could be due to the presence of intermolecular interactions, a change in the relaxation rate of the electronic spin, a structural distortion at low temperatures, or microcrystalline material present in the powder. On the basis of the Mössbauer spectra, which are consistent with an essentially axial system (*vide infra*), it is unlikely that a large structural distortion is responsible for this behavior. Our attempts to fully rationalize the very low temperature data (2−10 K) were unsuccessful, and therefore, our analysis of the HFEPR spectra of **2** relies on the data recorded at 30 K. Examination of the 2D frequency vs resonant field plot of Figure 3b reveals four branches where extrapolation of the frequency-dependent behavior of these transitions results in zero-field intercepts. These intercepts occur at 0, 90, 180, and 270 GHz. For an axial system with $S = {}^{7}/_{2}$ the zero field energies of the M_S states are given by $0D$ ($M_S = \pm 1/2$), $2D$ ($M_S = \pm 3/2$), $6D$ ($M_S = \pm 5/2$), and $12D$ ($M_S = \pm 7/2$). This means that the first four allowed ($\Delta M_S = \pm 1$) transitions occur at 0 (transitions within Kramers doublets), $2D$ ($M_S = \pm 1/2 \rightarrow \pm 3/2$), $4D$ ($M_S = \pm 3/2 \rightarrow \pm 5/2$), and $6D$ ($M_S = \pm 5/2 \rightarrow \pm 7/2$). These assignments and the equal spacing of zero-field gaps ($=2D$) are only possible if $E = 0$ and one also neglects higher-order ZFS interactions. The difference between each subsequently observed gap indicates that $2D \approx 90$ GHz or that $|D| \approx 1.5$ cm^{-1}. Examining the relative intensities of the x_1−x_7 transitions reveals that their amplitude decreases from low to high field (Figure 3c). This pattern is only possible when the x_1 transition originates from an M_S state that is lower in energy than the initial state of the x_2 transition. For this to occur requires that $D > 0$ (see Figure 3a). Spectral simulations that reproduce each individual spectrum (Figure 3c) as well as the global frequency versus applied field behavior (Figure 3b) confirm the sign of D. The field-dependent behavior of these transitions is parametrized by a modestly anisotropic $\tilde{\mathbf{g}}$ tensor, $g_{xy} = 2.04$ and $g_z = 2.00$. Given the relatively broad line widths in the recorded spectra of **2**, it is possible that a small E parameter is concealed within the line width. On the basis of the simulations of the zero-field energies as well as on the positions of the high-field resonances, we estimated an upper limit to the rhombic distortion of $E \leq 0.03$ cm^{-1} ($E/D \leq 0.02$).

HFEPR Spectra of ***3***. Absent a metal−metal bond, the formal oxidation states of the Fe sites in **3** are assigned as +3 (tris(phosphine) site) and +2 (tris(amide) site) with d^5 and d^6 electronic configurations, respectively. On the basis of previous magnetic susceptibility measurements, **3** was found to exhibit an intermediate-spin state and, thus, we analyzed the data using eq 1 with $S = 5/2$ (Figure 4a). The analysis of the HFEPR data obtained for **3** proceeded in a fashion similar to that of **2**. Zero-field intercepts were identified at 0 ($M_S = -1/2 \rightarrow +1/2$), ∼ 59 ($M_S = \pm 1/2 \rightarrow \pm 3/2$), and 110 GHz ($M_S = \pm 3/2 \rightarrow \pm 5/2$). We note that, due to the rhombicity (*vide infra*) of this system, these state assignments are not exact. However, using the dominant contribution to label the respective states provides us with a convenient handle for this discussion. In the axial limit ($E/D = 0$) the three lowest zero-field intercepts should occur at 0, $2D$, and $4D$. In this case, we observe a deviation from this splitting pattern, where the differences between subsequent zero-field intercepts are not equal. Such behavior is indicative of the presence of a rhombic or higher-order ZFS interaction. Given the large separation between spin states induced by the metal−metal bond, we expect higher-order ZFS to be absent or small and, thus, we have fit our data using only second-order ZFS interactions.[47] To a first approximation, the value of D is well constrained by the first gap, as well as the spacing between transitions z_5 (high-field limit: $M_S = -5/2 \rightarrow -3/2$) and z_4 (high-field limit: $M_S = -3/2 \rightarrow -1/2$). Since **3** possesses a half-integer spin, the rhombic anisotropy does not result in additional zero-field transitions such as those observed for **1**. However, the spacing of the zero-field transitions and the curvature of the frequency dependence trend are highly sensitive to E. In this case the strongest indication of the magnitude of E is the offset between peaks labeled x_{1-4} and y_{1-4}. These correspond, in the high-field limit, to the EPR allowed ($\Delta M_S = \pm 1$) transitions when the

https://dx.doi.org/10.1021/acs.inorgchem.0c02605
Inorg. Chem. 2020, 59, 18141−18155

magnetic field is applied parallel to the x/y components of the ZFS tensor. Fitting the overall frequency versus resonance field map, shown in Figure 4b, results in the following spin Hamiltonian parameters of the ground sextet state: $g_x = 2.03$, $g_y = 2.05$, $g_z = 2.00$, $D = +0.928$ cm^{-1}, and $E = 0.068$ cm^{-1} ($E/D = 0.073$). The sign of D is confirmed by an examination of the intensity pattern of the x/y_{1-4} peaks, where the highest intensities occur on the low-field side of $g = 2$. This is possible only when $D > 0$ (Figure 4a) and is supported by spectral simulations (Figure 4c). Additional HFEPR spectra for **1**−**3** are presented in Figure S2. Finally, we note that the superb quality of these spectra and resulting simulations offer one of the most accurately reported parametrizations for an anisotropic high-spin species.

High-Temperature Electron Paramagnetic Resonance of 2 and 3. The thermal isolation of ground spin states is a question of great interest in the molecular magnetism community. Therefore, we have attempted to investigate the separation of the ground state spin manifold from low-lying excited states by recording HFEPR spectra of **2** and **3** at elevated temperatures. For **2**, this measurement was performed at 220 K, and simulation of the 217.6 GHz spectrum was achieved with only minor changes to the low temperature spin-Hamiltonian parameters reported above (Figure 5). Given the sharper lines in **3**, we were able to record a strong spectrum at the higher temperature of 260 K. Again, we see no features that cannot be reproduced with an effective single-spin model. For both **2** and **3**, the slight changes in spin-Hamiltonian parameters likely result from minor structural changes driven by the increase in temperature. In both cases, the lack of spectral features not reproduced by the single-spin Hamiltonian parameters shows that the ground state spin is well isolated from the first excited state. This observation is fully consistent with the magnetic susceptibility measurements reported previously that showed a temperature-independent magnetic moment above ∼25 K, consistent with an isolated ground spin state.[19] Furthermore, the lack of observable influence from higher-order ZFS parameters illustrates that metal−metal-bonded systems may provide a route to suppress quantum tunneling of magnetization (QTM) induced by spin state mixing in polymetallic clusters.[7−11]

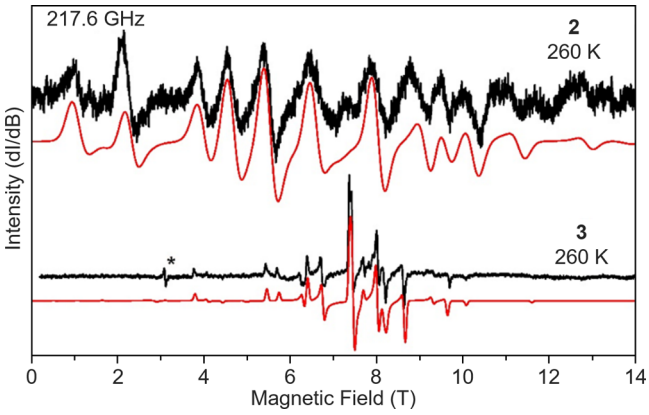

Figure 5. Experimental (black) and simulated (red) EPR spectra recorded at 220 and 260 K for compounds **2** and **3**, respectively. In the spectrum of **3** a rolling baseline was subtracted. The feature marked with an asterisk is a parallel mode transition, which is often observed in transmission spectra. The simulation parameters were as follows: for **2**, $g_x = 2.08$, $g_x = 2.08$, $g_z = 2.05$, $D = 1.58$ cm^{-1}, and $E = 0.00$ ($E/D = 0.00$); for **3**, $g_x = 2.03$, $g_x = 2.03$, $g_z = 2.02$, $D = 0.920$ cm^{-1}, and $E = 0.065$ cm^{-1} ($E/D = 0.070$).

^{57}Fe Nuclear γ Resonance (Mössbauer) Spectroscopy. With the electronic components of the spin-Hamiltonian determined via HFEPR, the parameters of the electron−nuclear interactions can be easily obtained from variable-field Mössbauer spectroscopy. The field-dependent spectra of **1**−**3** were analyzed using the following total spin-Hamiltonian, $\hat{H}_T$, which was obtained by augmenting eq 1 with terms describing the hyperfine interactions of the ^{57}Fe nuclei

$$\hat{H}_T = \hat{H}_{elec} + \hat{H}_{nuc} \tag{2}$$

$$\hat{H}_{nuc} = \sum_{\Theta} \left\{ \hat{\mathbf{S}} \cdot {}^{\Theta}\tilde{\mathbf{A}} \cdot {}^{\Theta}\hat{\mathbf{I}} + {}^{\Theta}\delta - g_n \beta_n \vec{\mathbf{B}} \cdot {}^{\Theta}\hat{\mathbf{I}} + \frac{eQ^{\Theta}V_{zz}}{4I(2I-1)} \left[3\,{}^{\Theta}\hat{I}_z^2 - \frac{15}{4} + {}^{\Theta}\eta\left({}^{\Theta}\hat{I}_x^2 - {}^{\Theta}\hat{I}_y^2\right) \right] \right\} \tag{3}$$

The index Θ (=N, P) accounts for each distinct Fe site in the molecule and, for **2** and **3**, will be labeled $^{N}\tilde{\mathbf{A}}$ for the tris(amide) Fe site or $^{P}\tilde{\mathbf{A}}$ for the tris(phosphine) Fe site. $^{\Theta}\tilde{\mathbf{A}}$ is the electron−nuclear hyperfine coupling tensor, g_n is the nuclear gyromagnetic ratio, β_n is the nuclear magneton, $^{\Theta}\hat{\mathbf{I}}$ is the nuclear spin operator of the individual iron sites (with components $^{\Theta}\hat{I}_\mu$, $\mu = x, y, z$), and $^{\Theta}\delta$ is the isomer shift. The quadrupole splitting, ΔE_Q, is related to the principal components of the electric field gradient (EFG) tensor by $\Delta E_Q = \frac{1}{2} eQV_{zz}\sqrt{1 + \eta^2/3}$ and $\eta = |V_{xx} - V_{yy}|/V_{zz}$, where e is the elementary charge, Q is the nuclear quadrupole moment, and $V_{\mu\mu}$ are the principal components of the EFG tensor in a coordinate system where $|V_{zz}| > |V_{xx}| > |V_{yy}|$. The parameters used for the first term in eq 2 were determined from the results of the HFEPR measurements, leaving only the terms in $\hat{H}_{nuc}$ to be determined. The observed field-dependent spectra result from an effective field, $\vec{\mathbf{B}}_{eff}$, acting on the ^{57}Fe nuclei. The magnitude of $\vec{\mathbf{B}}_{eff}$ results from the competition between the applied field, $\vec{\mathbf{B}}_{app}$, and the internal field produced by the unpaired electrons, $\vec{\mathbf{B}}_{int} = -\tilde{\mathbf{A}} \cdot \frac{\hat{\mathbf{S}}}{g_n \beta_n}$, so that $\vec{\mathbf{B}}_{eff} = \vec{\mathbf{B}}_{app} + \vec{\mathbf{B}}_{int}$. The spin expectation values predicted using eq 1 are presented in Figure S4.

^{57}Fe Mössbauer Spectra of 1. The zero-field spectra recorded for **1** at several temperatures between 4.2 and 180 K are nearly identical and consist of a single, well-defined quadrupole doublet (Figure S3a and Table S1). The 4.2 K, 0 T spectrum is best described using $\delta = 0.66$ mm/s and $\Delta E_Q = 2.05$ mm/s. These values are consistent with those reported previously at 110 K.[26] The temperature-independent parameters of this quadrupole doublet suggest that **1** has a single unique Fe site with an isolated orbital ground state (Figure S3a and Table S1). The zero-field Mössbauer parameters of **1** are typical for high-spin ferrous (Fe^{II}) complexes.[48] Figure 6a shows a series of field- and temperature-dependent spectra recorded for **1**. From HFEPR measurements, **1** was found to have a positive $D > \beta_e|\vec{\mathbf{B}}|$ ($\vec{\mathbf{B}}$ is the magnetic field vector), which implies a singlet, $M_S \approx 0$ ground state for all applied fields in these experiments (see Figure 2a). This scenario results in a low-temperature, field-dependent behavior that is dominated by A_x and A_y. This is due to the ability of a transverse field to mix the $M_S = \pm 1$ excited states into the

https://dx.doi.org/10.1021/acs.inorgchem.0c02605
Inorg. Chem. 2020, 59, 18141−18155

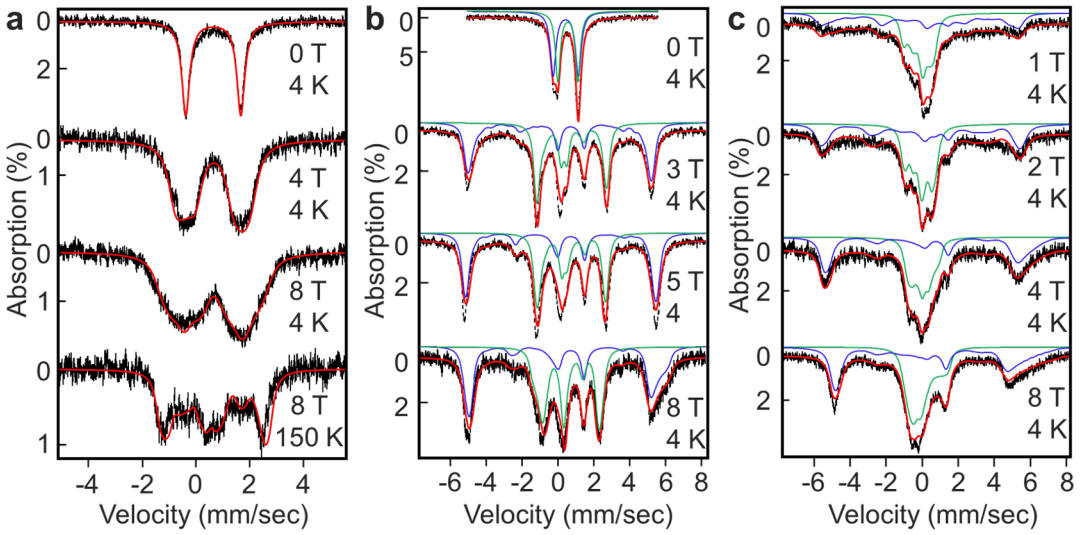

Figure 6. Experimental (black) and simulated (red) ^{57}Fe Mössbauer spectra of **1** (a), **2** (b), and **3** (c) at varying applied fields and temperatures. In (b) and (c) the blue trace corresponds to the tris(amide) Fe site, the green trace corresponds to the tris(phosphine) site, and the red trace is the summation of two sites. All simulations used the spin Hamiltonian parameters reported in Table 1.

ground M_S = 0 state. This mixing yields a nonzero value for $\langle \hat{S}_{x,y} \rangle$, while $\langle \hat{S}_z \rangle$ remains essentially null due to the large separation of the first excited state from the ground state (Figure 2a and Figure S4). To evaluate the magnitude of A_z, higher magnetic fields and variable-temperature measurements were required. Moreover, to ascertain the sign of ΔE_Q and the magnitude of η, spectra were collected at elevated temperatures, where we anticipate a Curie-like behavior, $\langle \hat{S} \rangle \approx 1/T$, such that the contribution of $\vec{\mathbf{B}}_{int}$ is sensitive mainly to the nuclear-Zeeman and quadrupolar interactions. Fits of the 150 K, 8 T spectrum revealed that ΔE_Q is negative and η = 0.8. We have simulated the full set of experimental spectra in a fast-relaxation regime, and our best fit is achieved with A_x = −5.5 MHz, A_y = +0.4 MHz, and A_z = −45.5 MHz, as shown in Figure 6a.

^{57}Fe Mössbauer Spectra of ***2***. Between 80 and 180 K the zero-field spectra of **2** are adequately described as consisting of a single broad quadrupole doublet with asymmetrically broadened resonances (Figure S3b). When the temperature is lowered to 4.2 K, the spectrum sharpens and reveals two distinct quadrupole doublets with $\delta/\Delta E_Q$ = 0.56/1.11 mm/s for ^{N}**2** and 0.44/1.41 mm/s for ^{P}**2** (*vide infra*). The observation of quadrupole doublets with narrow line widths implies that, at 4.2 K, the electronic spin is in a fast-relaxation regime: that is, a spin-flip rate $\omega \geq 10^{11}$ Hz.[48] For Kramers systems such as **2**, a slow relaxation rate ($\omega \leq 10^8$ Hz) is expected to lead to spectra that exhibit a magnetic hyperfine splitting even in zero field. Consequently, these observations demonstrate that the broadening of the zero-field spectra observed at high temperatures is not relaxational in nature, that is, it is not due to the presence of an unresolved magnetic hyperfine splitting. This unusual behavior might be indicative of a temperature-induced structural change that redistributes the electron density between the two individual iron sites or the recoilless fraction of one of the sites changes at a different rate with temperature in comparison to the other. Regardless of the high-temperature behavior, the observation of two unique quadrupole doublets at 4.2 K is consistent with the expectation that the different ligand fields impart a unique nuclear environment for each Fe site (Figure 6b). An analysis of the HFEPR data demonstrated that **2** exhibits an $M_S \cong \pm 1/2$ Kramers doublet ground state. However, because $D \approx \beta_e|\vec{\mathbf{B}}|$, when $\vec{\mathbf{B}}$ is parallel to the z component of the ZFS tensor, the M_S value of the ground state will change as the field is increased (see Figure 3a, top). Therefore, the evolution of the spectral features under varying applied fields is sensitive to all three principal components of the $\tilde{\mathbf{A}}$ tensors (since both $\langle \hat{S}_{x,y} \rangle$ and $\langle \hat{S}_z \rangle \neq 0$; see Figure S4b). We find that the spectra can only be fit by considering two unique $\tilde{\mathbf{A}}$ tensors. The overall spectrum can be deconvoluted into two contributions, each associated with an individual iron site. An examination of the spin expectation values, shown in Figure S4b, reveals that at low temperature and fields between 1 and 3 T the theoretical spectra are very sensitive to $^{N/P}A_x$ and $^{N/P}A_y$. Reproducing the extent of the hyperfine splitting for this field range offers a strong constraint on these parameters. An inspection of Figure 6b reveals that the two spectral components associated with the individual iron sites exhibit markedly different field-dependent behaviors. This can be appreciated by comparing the average values of the $\tilde{\mathbf{A}}$ tensors, A_{iso}, where the A_{iso} value of ^{P}**2** is less than half that of the ^{N}**2** site ($^{N}A_{iso}$ = −17.7 MHz vs $^{P}A_{iso}$ = −7.6 MHz; see below for assignment). As in **1**, we can exploit the Curie-like behavior of **2** at high temperatures and, in doing so, find that ΔE_Q is negative for ^{P}**2** and positive for ^{N}**2** and that $\eta \approx 0$ for both sites (Figure 6b and Figure S5).

^{57}Fe Mössbauer Spectra of ***3***. The zero-field spectrum recorded at 80 K for **3** exhibits a single well-defined quadrupole doublet parametrized by $\delta/\Delta E_Q$ = −0.07/0.57 mm/s (Figure S3c) and is consistent with the previously reported spectrum at 90 K.[19] This result may suggest a fully delocalized electron distribution associated with the two Fe ions. However, given the significantly different ligand field environments at the individual sites, this scenario seems unlikely. A previous study calculated the $\delta/\Delta E_Q$ values for each site of **3**.[19] These calculations predicted that, as expected, the two Fe sites should indeed be inequivalent. Therefore, to discover the spectral signature of the "missing" Fe, we have performed a series of temperature- and field-dependent measurements. Superficially, the zero-field spectra recorded

https://dx.doi.org/10.1021/acs.inorgchem.0c02605
Inorg. Chem. 2020, 59, 18141−18155

Table 1. Spin Hamiltonian Parameters Extracted From HFEPR and ^{57}Fe Mössbauer Measurements for 1−3[a] and Comparable Literature Examples

compound	S	D (cm^{-1})	E/D	$[g_x, g_y, g_z]$	δ (mm/s)	ΔE_Q (mm/s)	η	A_x (MHz)	A_y (MHz)	A_z (MHz)	A_{iso} (MHz)	ref
1	2	13.24(4)	0.014(2)	[2.24(2), 2.25(2), 2.00(2)]	0.66(1)	−2.05(3)[b]	0.8(2)	−5.5(7)	+0.4(4)	−45.5(3)	−16.9	this work
^{P}**2**	7/2	1.50(3)	0.00(1)	[2.04(2), 2.04(2), 2.00(2)]	0.56(2)	−1.11(4)	0.0(1)	−6.6(2)	−5.9(2)	−10.4(5)	−7.6	this work
^{N}**2**					0.44(2)	1.41(4)	0.0(1)	−14.8(3)	−15.6(3)	−22.8(5)	−17.7	
^{P}**3**	5/2	0.928(3)	0.073(2)	[2.03(1), 2.05(1), 2.00(1)]	−0.04(1)	0.51(2)	0.0(1)	−4.3(3)	−3.1(3)	0.2(2)	−2.4	this work
^{N}**3**					0.39[c]	2.14[c]	0.0[c]	−18.8[c]	−20.3[c]	−24.8[c]	−21.3	
FeS_3 (**4**)[d]	2	10.2(5)[j]	0[j]	[2.2, 2.2, 2][l]	0.56	−0.83	0	−7.5(4)	−7.5(4)	−29.5(14)	−14.9	49
FeS_3 (**5**)[d]	2	14(3)[j]	0.25[j]		0.60	−0.87[m]	0.93(7)	−3.9	+4.5	−36(4)	−11.8	49
FeN_3[e]	2	9.9[i]	0.0[i]	[2.18, 2.18, 1.91][i]	0.59	0.60						50
Fe_2L_3[f]	7/2	8.2[i]	0.0[i]	2[i]	0.65	0.32	0	−15.89	−14.53	−42.26		51
LFe_{2P}[g]	7/2	±4.29[i,k]	0[i]	1.96[i]	0.55	−0.12				−7.0		20
LFe_{2N}[g]					0.42	−0.13				−16.2		
LFe_2-Cl_P[h]	7/2	−2.3(5)[j]	0[j]		0.77	0.13				−9.6		20
LFe_2-Cl_N[h]					0.50	0.12				−16.9		

[a] A = 1 MHz corresponds to $A/g_n\beta_n$ = 0.729 T. A blank value in the table indicates that the parameter was not determined or not explicitly given in the manuscript. In all cases above, δ, ΔE_Q, η, and A values were determined by ^{57}Fe Mössbauer spectroscopy. Values in parentheses are the estimated uncertainties in the last digit. [b] EFG is rotated: α_{EFG}, β_{EFG} = 65°, 35° [c] See main text for discussion of estimated uncertainty. [d] $[Ph_4P][Fe(SC_6H_3\text{-}2,4,6\text{-}{}^tBu_3)_3]\cdot 2MeCN\cdot C_7H_8$ (**4**) and $[Li(THF)_2\ Fe(SC_6H_3\text{-}2,4,6\text{-}{}^tBu_3)_3]\cdot 1/2C_6H_{14}$ (**5**). [e] $[Li(15\text{-crown-}5)][Fe\{N(SiMe_3)_2\}_3]$. [f] Diiron tris-(diphenylformamidinate). [g] Fe_2L (L = $N(o\text{-}C_6H_4NHCH_2P^iPr_2)_3$). [h] $Li(THF)_3[LFe_2Cl]Li(THF)_3$. [i] Parameter determined by SQUID magnetometry. [j] Parameter determined by ^{57}Fe Mössbauer spectroscopy. [k] In this case the authors state that the value is not well determined due to intermolecular interactions. Furthermore, the value is reported as an absolute value. [l] These values were estimated by relating D and E to the g values with the assumption that contributions from S = 1 states were negligible. [m] EFG is rotated: α_{EFG} = 60°.

https://dx.doi.org/10.1021/acs.inorgchem.0c02605
Inorg. Chem. 2020, 59, 18141−18155

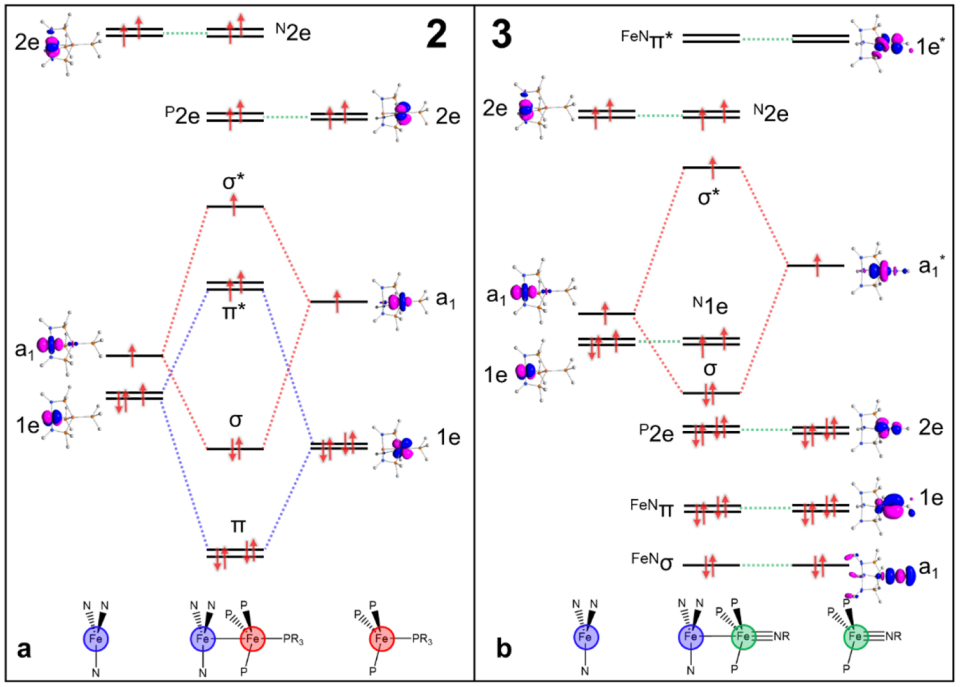

Figure 7. Qualitative MO energy level diagrams for **2** (a) and **3** (b). The color highlighting each metal ion is indicative of the formal oxidation state of each site, absent any metal−metal bonding interactions: red (+1), blue (+2), and green (+3). For each orbital of e symmetry we show only one representative orbital.

at temperatures from 4 to 250 K exhibit a single, essentially temperature independent, quadrupole doublet (Figure S3c and Table S1). However, a careful examination of the low-temperature data reveals substantial broad features that extend to either side of the central doublet up to ±6 mm/s. Moreover, the field-dependent measurements performed at 4.2 K show a gradual, field-induced increase in the intensity of this second spectral component (Figure 6c and Figure S6). These observations show that the "missing" spectral component is, in fact, present except that it exhibits a large magnetic hyperfine splitting, even in zero field. The latter observation is consistent with the behavior expected for Kramers systems in a slow-relaxation regime. From this perspective, the observation of a quadrupole doublet at 4.2 K is unusual. Our analysis suggests that it originates from an iron site with a nearly null hyperfine coupling tensor which, in turn, leads to a vanishing internal field for that site. Inspection of Figure 6c shows that the increase in the intensity of the hyperfine-split spectral component upon an increase in the strength of the applied field is due to depopulation of the excited spin sublevels. In a slow-relaxation regime each spin sublevel exhibits an associated Mössbauer spectrum with an intensity proportional to its Boltzmann population and magnetic hyperfine splitting determined by the spin expectation value of that microstate (see Figure S4c).

Variable-field measurements showed that the largest magnetic hyperfine splitting is observed at ∼2 T. This saturation field agrees well with the spin expectation values calculated using the spin-Hamiltonian parameters determined via HFEPR (Figure S4c), assuming a slow-relaxation regime. Just as for **2**, the extent of the magnetic hyperfine splitting near saturation offers a strong constraint on $^{P/N}A_x$ and $^{P/N}A_y$. Additionally, the $^{P/N}A_z$ components were estimated from the high-field, $|\mathbf{B}| \geq 4$ T, data for which $\langle \hat{S}_z \rangle = -2.5$. Our analysis was complicated by the presence of two distinct iron ions. However, by performing extensive simulations, we could delineate the individual spectral components associated with each site. Again, we observe one site with significantly smaller $\tilde{\mathbf{A}}$ tensor components than the other. We note that because the electronic spin exhibits an intermediate-relaxation regime at all temperatures higher than 4.2 K, we were unable to derive precise values for the $\delta/\Delta E_Q$ and $\tilde{\mathbf{A}}$ values of $^{N}\mathbf{3}$. Regardless, our simulations suggest that the experimental values of $\delta/\Delta E_Q(^{N}\mathbf{3})$ are within 0.1/0.5 mm/s and the $^{N}\tilde{\mathbf{A}}$ tensor components are within 10% of those quoted in Table 1.

DISCUSSION

Qualitative Bonding Diagram. To explore how the Fe−Fe bonding interactions in **2** and **3** might affect the orbitals of the individual magnetic sites, we have constructed a series of qualitative molecular orbital (MO) energy level diagrams (Figure 7). To elucidate the relative orbital energies at each metal site, prior to the formation of a metal−metal bond, we have performed CASSCF calculations on model compounds where a diamagnetic metal analogue replaces one of the Fe ions. In this way, we ascertained the expected orbital orderings and their relative energies. Here, we have defined the molecular z axis to be coincident with the approximate 3-fold rotation axis. In **1**, and absent the metal−metal interaction in **2** and **3**, the tris(amide)-coordinated site is formally assigned as Fe(II) (d^6), with five d orbitals split into a singlet a_1 $\{z^2\}$, and two doublets, 1e $\{yz, xz\}$ and 2e $\{xy, x^2 - y^2\}$ (Figure 7). Interestingly, while for **1** we find that the a_1 orbital is lowest in energy (*vide infra*), for our single-Fe models of **2** and **3**, 1e is lowest. In **2** and **3** the $\sim C_{3v}$ tris(phosphine) coordination splits the d orbitals into a singlet (a_1 $\{z^2\}$) and two doublets (1e, 2e) (right sides of Figure 7). However, in this case, the two doublets are mixtures of the $\{yz, xz\}$ and $\{xy, x^2 - y^2\}$ orbitals due to the displacement of the Fe atom from the plane formed by the three P atoms.

https://dx.doi.org/10.1021/acs.inorgchem.0c02605
Inorg. Chem. 2020, 59, 18141−18155

For **2** the apical PR_3 group destabilizes the a_1 orbital of the phosphine-bound Fe atom, resulting in the 1e doublet having the lowest energy. On the basis of our calculations and the point charge model presented in a previous report,[36] we expect that the lowest energy orbitals at both sites will have significant xz/yz character. This allows for some degree of π-bonding interaction between the two sites. However, due to the different ligand field environments, the metal−metal bond will be highly polarized. Similarly, the a_1 orbitals of the individual iron sites may also mix, forming a polarized σ-bond. Given the reduced metal−ligand overlap of the tris(phosphine) site in comparison to the tris(amide) site, we expect the metal orbitals of δ symmetry to be energetically separated and to remain essentially nonbonding (see Figure 7).

The terminal imido group of **3** presents a more complicated bonding pattern that is not easily rationalized by considering a simple point charge model. We start by taking into account the formation of the Fe≡NR moiety, which generates one set of bonding/antibonding orbitals of σ symmetry and two sets of π symmetry (Figure 7b). Note that, while the e (p_x/p_y) orbitals of the NR group have a larger overlap with the 1e group (predominately xz/yz), there may also be some stabilizing interaction with the 2e group of the ^{P}Fe (predominately $xy/x^2 - y^2$). The main consequence of these strong π interactions is that the orbitals of 1e* symmetry, with most of the metal character, are greatly destabilized, while the 2e doublet acquires a marginal degree of stabilization. This orbital rearrangement will disrupt the formation of the π bond by effectively inverting the relative energies of the 1e ($\sim\{yz, xz\}$) and 2e ($\sim\{xy, x^2 - y^2\}$) orbitals in comparison to the case in **2**. Our qualitative bonding pictures of **2** and **3** are supported by CASSCF calculations of the ground states (Figures S7 and S8).

DFT-Predicted Ground State Electronic Configurations and ^{57}Fe Hyperfine Parameters. To rationalize the observed hyperfine splitting parameters determined using Mössbauer spectroscopy, we have employed DFT to derive predicted δ, ΔE_Q, and η values and the $\tilde{\mathbf{A}}$ tensors for **1**−**3** (see Tables S2−S4).

Electronic Structure of ***1***. Analyses of the gross orbital population and reduced Mulliken orbital charges predicted for **1** (Table S5) reveal a ground state electronic configuration for which the single spin-down, β electron of the iron(II) ion is accommodated in an orbital composed of a mixture of z^2 and xz. The isomer shift value of **1**, δ^{exp} = 0.66 mm/s, is typical of high-spin Fe(II) sites and is similar to those reported for other three-coordinate compounds.[49,50] However, the predicted value, δ^{calc} = 0.50 mm/s, is 0.16 mm/s smaller than the experimental value. Although this difference is larger than anticipated (we expected an error of ≤0.10 mm/s), this observation is not unprecedented for low-coordinate systems.[52] A previous investigation of iron(II) complexes supported by β-diketiminate ligands suggested that the theoretical isomer shift values of three-coordinate compounds that have a z^2 ground state are exquisitely sensitive to the population of the 4s orbitals and to the strength of the spin−orbit coupling.[53] Unlike the case for other 3d orbitals, the mixing of the 4s orbital with z^2 is symmetry-allowed, leading to a higher electronic density at the nucleus and, thus, to a reduced isomer shift. Considering that for **1**, the spin−orbit coupling is relatively modest, the low predicted isomer shift value suggests that DFT calculations overestimate the 4s contribution to the ground state (see Tables S2−S5).

One of the most puzzling features of **1** is that, while its ZFS and $\tilde{\mathbf{A}}$ tensors are nearly axial, the EFG tensor is rhombic with a rather large asymmetry parameter, $\eta^{exp} \approx 0.8$. Interestingly, this behavior is reproduced by our calculations, which predict η^{calc} = 0.75, $E \approx 0$, and $A_x \approx A_y \ll A_z$. We anticipated that the approximate 3-fold symmetry of iron's first coordination sphere would lead to axial tensors, including the EFG, for which the z component is aligned with the C_3 rotation axis. Moreover, iron(II) sites with planar geometries typically have a small quadrupole splitting which originates from the competition between the ligand (ν^{lig}) and valence (ν^{val}) contributions to the EFG, $\nu = \nu^{lig} + \nu^{val}$ (we use ν for $eQV_{zz}/2$), which have opposite signs. The valence contribution of a z^2 ground state is roughly $(\nu_{xx}^{val}, \nu_{yy}^{val}, \nu_{zz}^{val}) \approx (2, 2, -4)$. When the ligands are idealized as point charges and are placed in a planar-trigonal arrangement, ∼2 Å away from the metal, we anticipate the ligand contribution $(\nu_{xx}^{lig}, \nu_{yy}^{lig}, \nu_{zz}^{lig}) \approx (-1.5, -1.5, +3)$. Therefore, we should observe a value, $\Delta E_Q \approx -1.0$ mm/s, which is considerably smaller than those expected for typical high-spin ferrous ions. Interestingly, the ΔE_Q = −0.83 mm/s and $|\Delta E_Q|$ = 0.60 mm/s values respectively observed for $[Fe(SR)_3]^-$ (R = C_6H_2-2,4,6-tBu_3) reported by Sanakis et al.[49] and for $Fe(N(SiMe_3)_2)_3$ described by Eichhöfer et al.[50] suggest that the simple arguments presented above are essentially valid. To elucidate the larger than expected ΔE_Q = −2.05 mm/s and η = 0.8 values observed for **1**, we have evaluated the predicted EFG tensors of a series of simplified theoretical models derived from the experimental crystal structure. An inspection of Table S6 shows that when only the first coordination sphere is considered the predicted EFG tensor is indeed quasi-axial, i.e., we obtain η^{calc} = 0.05 for $[Fe(NH_2)_3]^-$. Subsequent inclusion of the phosphino groups (PH_2) and of the $Cu_2(HNPH_2)$ moiety leads to a progressive increase in the asymmetry of the EFG tensor. We obtained η^{calc} = 0.51 for $[Fe(HNPH_2)_3]^-$ and 0.84 for $FeCu_2(HNPH_2)_4$, respectively. Therefore, the high η value for **1** is induced by the second coordination sphere of the iron ion, i.e. it can be traced to the increased displacement of the z^2 orbital from the normal to the FeN_3 plane, mediated by the mixing with the xz orbital and to the misalignment of the ligand and valence contributions to the EFG tensor (see Table S6).

Because of the nonzero $\langle z^2|\hat{L}_x|yz\rangle = -\langle z^2|\hat{L}_x|xz\rangle = i\sqrt{3}$ matrix elements, the two lowest excited orbital states of **1**, corresponding to $\{z^2 \rightarrow xz/yz\}^{\beta}$, are mixed into the ground state by the spin−orbit coupling interaction (*vide infra*). The similarity of their energies leads to a quasiaxial ZFS tensor and a predicted orbital contribution to the hyperfine coupling tensor ($\tilde{\mathbf{A}}_L$). We note that the DFT-predicted D value (D^{calc} = 2.89 cm^{-1}) is severely underestimated by our theoretical method. The isotropic hyperfine coupling constant obtained by taking the average of the principal components of the $\tilde{\mathbf{A}}$ tensor, often used in the evaluation of spin coupling schemes, A_{iso}^{calc} = −17.1 MHz, is in good agreement with the experimental value A_{iso}^{exp} = −16.9 MHz. Moreover, this value is very similar to that of $[Fe(SR)_3]^-$ (R = C_6H_2-2,4,6-tBu_3), which was shown to have A_{iso} = −14.9 MHz.[49]

Electronic Structure of ***2***. The predicted isomer shifts for ^{N}**2** and ^{P}**2** of 0.36 and 0.42 mm/s, respectively, reproduce the relative magnitudes but underestimate both by ∼0.1 mm/s in comparison to the respective experimental values of 0.44 and 0.56 mm/s. The isomer shift of ^{N}**2** is smaller than that of **1**, which means that there is an increased s electron density at the nucleus of ^{N}**2** in comparison to **1**. This change is likely induced

https://dx.doi.org/10.1021/acs.inorgchem.0c02605
Inorg. Chem. 2020, 59, 18141−18155

by the metal−metal bonding interaction. A similar effect and explanation were given in a study by Miller et al., where they observed that the isomer shifts in Fe−Co compounds were lower than in the analogous Fe−Fe compounds.[20] As expected from the approximate 3-fold symmetry of the complex, the calculated ν_{zz} component of the EFG for each site of **2** was predicted to be collinear with the axis formed by the Fe−Fe bond and was found to be negative for ^{P}**2** and positive for ^{N}**2**. Moreover, the calculated values of ΔE_Q and η are in excellent agreement with our experimental results. The calculated Fermi contact contributions are $^{P}\tilde{\mathbf{A}}^{calc}_{FC}$ = −4.84 MHz and $^{N}\tilde{\mathbf{A}}^{calc}_{FC}$ = −9.94 MHz, which immediately suggests that the main reason the two hyperfine tensors are unique is because the iron sites have different spin densities. Just like the EFG tensors, the approximate C_3 symmetry of **2** leads to axial $\tilde{\mathbf{A}}$ tensors. For each site, the single negative component of the dipolar contribution to the $\tilde{\mathbf{A}}$ tensor ($\tilde{\mathbf{A}}^{calc}_{dip}$) adds to the Fermi contact in A_z, while the two smaller positive components oppose the Fermi contact for $A_{x/y}$. The $\tilde{\mathbf{A}}_L$ contribution to $^{N}\tilde{\mathbf{A}}$ is essentially quenched along the z direction and opposed to the Fermi contact along x/y. Interestingly, we find that the $\tilde{\mathbf{A}}_L$ contribution to $^{P}\tilde{\mathbf{A}}$ is almost isotropic and opposes $\tilde{\mathbf{A}}_{FC}$ in all three principal components of the $^{P}\tilde{\mathbf{A}}$ tensor.

There have been two compounds directly comparable to **2** (Fe−Fe bond, S = 7/2) reported in the literature. The first is $Fe_2(DPhF)_3$ (DPhF = diphenylforamidinate), in which the ligand field of each iron site is the same.[51] In this case, only a single δ, ΔE_Q, and $\tilde{\mathbf{A}}$ tensor (Table 1, Fe_2L_3) are observed, since the identical local symmetries promote nonpolarized σ, π, and even δ interactions. Here the single observed isomer shift of 0.65 mm/s is slightly higher than for either site in **2**. The other reported compound is Fe_2L, where L is a tris(phosphineamido)amine ligand, which engenders a unique ligand field at each Fe site, similar to that of **2**.[20] In this case, two distinct values of δ, ΔE_Q, and the $\tilde{\mathbf{A}}$ tensors (Table 1) are required to fit the experimental results. As for **2**, the dissimilar ligand environments result in highly polarized bonds, as well as nonbonding orbitals that enforce a unique nuclear environment at each site. While the δ values in Fe_2L are essentially identical with those of **2**, the quadrupole splitting parameters are ∼0.1 mm/s, significantly smaller than those observed here.

Electronic Structure of **3**. The most striking feature in the parameter set of **3** is the negative isomer shift. While unusual, negative isomer shifts have been reported for several highly oxidized Fe centers as well as in low-spin Fe(III) compounds.[54−57] Notably, several of the reported species with negative isomer shifts contain imido ligands. Given these observations, we have assigned this parameter set to the ^{P}**3** site. This observation is confirmed by DFT calculations, which reproduce the negative isomer shift as well as the small, positive quadrupole splitting. The isomer shift and quadrupole splitting of the ^{N}**3** site are similar to those observed in **2**, but due to the slow relaxation of **3**, we are unable to resolve the quadrupole doublet and corresponding isomer shift of ^{N}**3** to the same level of accuracy as for **2**. We again find that the calculated ν_{zz} component of the EFG for both the ^{N}**3** and ^{P}**3** sites are collinear with the Fe−Fe bond. We find that incorporating a nonzero η value in our simulations results in no improvement in the quality of the fit and, therefore, we experimentally assign η = 0. The experimentally determined hyperfine tensor of ^{N}**3** is like that of ^{N}**2** but has a slight rhombicity. The ^{P}**3** site displays a remarkably small A_{iso} value of −2.4 MHz, which is in excellent agreement with the DFT-derived value of −1.81 MHz, where the calculated Fermi contact contribution is $^{P}\tilde{\mathbf{A}}^{calc}_{Fc}$ = −1.94 MHz. The calculated $\tilde{\mathbf{A}}^{calc}_{dip}$ and $\tilde{\mathbf{A}}^{calc}_{L}$ contributions are nearly identical between ^{N}**2** and ^{N}**3**. Meanwhile, in ^{P}**3**, the single negative component of $\tilde{\mathbf{A}}^{calc}_{dip}$ opposes the Fermi contact in A_z, while the two smaller positive components augment the Fermi contact in $A_{x/y}$, opposite to the observation at the other site. The $\tilde{\mathbf{A}}^{calc}_{L}$ contribution to $^{P}\tilde{\mathbf{A}}$ is essentially quenched with only a small contribution to A_z. There are few metal−metal-bonded systems in the literature that also contain metal−ligand multiple bonds, and to our knowledge, no other variable-field Mössbauer studies have been performed on similar species. The full listing of the DFT calculated Mössbauer parameters along with the calculated spin densities and structural comparisons of the ^{N}Fe sites are shown in Tables S2−S7 and Figure S9 in the Supporting Information.

Physical Origin of Zero-Field Splitting. To investigate the electronic origin of the ZFS parameters in **1**−**3**, we have calculated the $\tilde{\mathbf{D}}$ tensor using SA-CASSCF/NEVPT2. To analyze the results of these calculations, it is useful to relate them to ligand field theory. In transition-metal-based systems the dominant contribution to the ZFS is generally due to the spin−orbit coupling interaction. Using the second-order perturbation formalism, the components of the $\tilde{\mathbf{D}}$ tensor (for excited states with the same spin as the ground state) may be determined by

$$D_{\mu\nu} = -\frac{1}{S^2}\sum_{b(S=S_g)}\Delta_b^{-1}\left\langle \Psi_g^S\left|\sum_{i,\Theta}{}^{\Theta}\zeta^{\Theta}\hat{l}_{i,\mu}\hat{s}_{i,z}\right|\Psi_b^S\right\rangle \left\langle \Psi_b^S\left|\sum_{i,\Theta}{}^{\Theta}\zeta^{\Theta}\hat{l}_{i,\nu}\hat{s}_{i,z}\right|\Psi_g^S\right\rangle \quad (4)$$

where $D_{\mu\nu}$ is a Cartesian component of the $\tilde{\mathbf{D}}$ tensor, ${}^{\Theta}\zeta_i$ is the one-electron spin−orbit coupling constant for the Θ nucleus, Δ_b is the energy separation between the ground (Ψ_g^S) and b^{th} (Ψ_b^S) excited state, and ${}^{\Theta}\hat{l}_i$ is the Cartesian component of the orbital angular momentum operator relative to electron i, and S_g is the spin associated with the ground state.[58] The components of the $\tilde{\mathbf{D}}$ tensor given by eq 4 are related to the ZFS parameters D and E by $D = D_{zz} - 1/2(D_{xx} + D_{yy})$ and $E = 1/2(D_{xx} - D_{yy})$; here $|D_{zz}| > |D_{yy}| > |D_{xx}|$. From the CASSCF-derived qualitative MO splitting for **1** presented in Figure 8, we find a predominant z^2 orbital ground state with some admixture of xz character. As expected from the perturbation theory (see eqs S1 and S2 in the Supporting Information obtained by assuming a pure z^2 orbital) the *ab initio* calculations reveal substantial contributions to the $\tilde{\mathbf{D}}$ tensor from the two lowest quintet states (Figure 8). An important conceptual difference between the $\tilde{\mathbf{g}}$ and $\tilde{\mathbf{D}}$ tensors is that contributions to $\tilde{\mathbf{g}}$ arise only from states with the same total spin as the ground state, while contributions to $\tilde{\mathbf{D}}$ can also come from states with spin $S = S_g$ or $S = S_g \pm 1$. Thus, eq 4 can be augmented with expressions for the contributions from states with $S = S_g \pm 1$ to obtain a more complete expression for D.[59] However, given the similarity of the expressions for the $\tilde{\mathbf{g}}$ tensor and eq 4, it is possible to assess the contributions to D from states with different spin by relating the ZFS parameters to the g values (see eqs S1 and S2). Since the g values of **1** are known to a high degree of precision, we estimate the contribution of triplet states, ${}^{T}D$, to the axial ZFS parameter, D, by combining eqs S1 and S2, resulting in

https://dx.doi.org/10.1021/acs.inorgchem.0c02605
Inorg. Chem. 2020, 59, 18141−18155

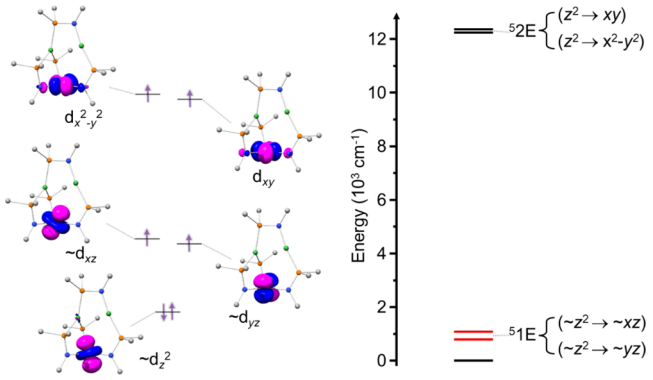

Figure 8. (left) Qualitative MO diagram resulting from a SA-CASSCF/NEVPT2 calculation for **1** depicting the dominant configuration of the ground state. (right) Energies of the low-lying excited states where the red lines correspond to the states that contribute to D. In this case, both indicated states have positive contributions. Here, the triplet states are omitted for clarity and are calculated to span ~16000−68000 cm^{-1}.

$$^{T}D \approx D - \left\{ \frac{\zeta}{8}(g_{\perp} - g_{e}) \right\} \quad (5)$$

where D and $g_{\perp}$ are the experimentally determined value of D and the average of g_x and g_y, respectively. Using $g_{\perp} - g_e = 0.245$ and $\zeta = 400$ (~95% of the free ion value), we estimate that $^{T}D \approx 0.99$ cm^{-1} or 7.5% of the experimentally determined D. We can compare these results to the CASSCF/NEVPT2 calculation, which predicts $D^{calc} = 20.15$ cm^{-1} and $E/D = 0.07$, where ^{T}D contributes ~11% to the second-order zero-field splitting parameter, D. The calculated magnitude of D is in reasonable agreement with the experimental value ($D^{exp} = 13.24$ cm^{-1}). The disagreement between experimental and calculated D values likely means that the energies of the 1E states are underestimated in the *ab initio* calculations. This CASSCF/NEVPT2 ^{T}D value is in good agreement with that predicted by the simple ligand-field model described in Figure S10 ($^{T}D = 2.1$ cm^{-1}).

A qualitative MO diagram of **2**, showing the predominant ground state configuration as determined by a SA-CASSCF/NEVPT2 calculation, is shown in Figure 9. Before we examine the *ab initio* results, it is instructive to reframe the problem in a more familiar qualitative molecular orbital theory. In the case of a single magnetic ion, the expressions for D are rather compact and are easily derived. The combination of two spin-bearing sites, strong bonding interactions, and numerous low-lying excited states in **2** and **3** make similar expressions unpractical and cumbersome. However, we can rationalize the sign of D by examining how the excited states couple to the ground state. States that couple through $\hat{L}_z$ (this operator acts on the state rather than the single electron as in eq 4) will contribute to a negative overall D parameter, while states that couple through $\hat{L}_x/\hat{L}_y$ will make a positive contribution to D. As described above, D is also affected by states where $S = S_g \pm 1$. In these cases, the signs of contributions are inverted such that those that couple through $\hat{L}_z$ are positive and those through $\hat{L}_x/\hat{L}_y$ are negative. The SA-CASSCF/NEVPT2 ZFS values calculated for **2** are $D = +3.42$ cm^{-1} and $E = 0.00$ cm^{-1}, which are in reasonable agreement with experiment ($D = +1.50$ cm^{-1} and $E = 0.00$ cm^{-1}). The resulting low-lying excitations are shown in Figure 9. The largest predicted contribution originates from the $\sigma \rightarrow \pi$ transition ($A_2 \rightarrow E$) with $S = S_g$ and, as expected from group theory arguments (the z (x,y) component of the SOC operator transforms as A_2 (E)), results in a positive contribution to D. All states that interact with the ground state via spin−orbit coupling, along with their contribution to D, are recorded in Table S8. Summing the contributions of the individual octet states, we find that they yield ~110% of the actual value of D, while the sextet states contribute ~−10% to the value of D. The value of D for **2** is significantly smaller than that of **1** due to the inevitable reduction that occurs upon projecting the single-site anisotropies onto the coupled molecular spin state. It is likely possible to significantly increase the ZFS by designing systems with orbital degeneracy (a more detailed explanation will be given below).

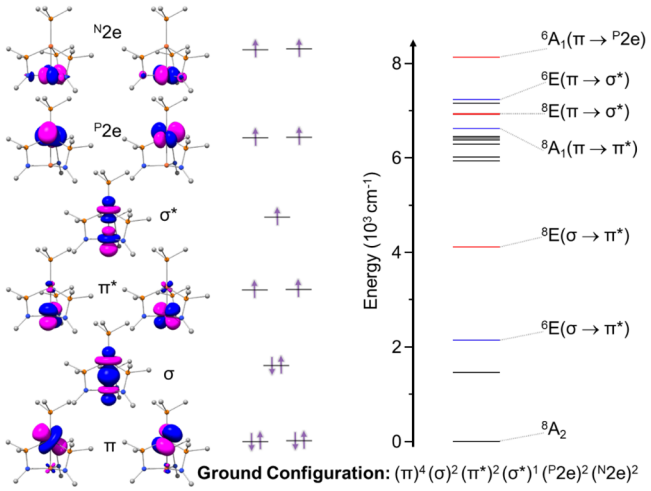

Figure 9. (left) Qualitative MO diagram for **2** resulting from a SA-CASSCF/NEVPT2 calculation depicting the dominant configuration of the ground state. (right) Energies of the first 10 octet and first 10 sextet states, where the labels correspond to the Mulliken symbol of the indicated state with the single excitation that describes the main configuration in parentheses. For clarity, only states with contributions to D > 1% of the total value are labeled. The ground state is labeled with the dominant configuration. The lines representing the energies of the states are colored according to their contribution to D: red (positive), blue (negative), and negligible/zero (black). Increasing the number of roots to 30 of each spin state resulted in essentially no change in the calculated ZFS parameters (Table S9).

The SA-CASSCF/NEVPT2 ZFS values calculated for **3** are $D = +1.57$ cm^{-1} and $E = 0.24$ cm^{-1} ($E/D = 0.15$). Although the rhombicity is overestimated, these values are in good agreement with experiment ($D = +0.928$ cm^{-1} and $E = 0.068$ cm^{-1}). The resulting low-lying excitations and qualitative MO diagram are shown in Figure S11. Unfortunately, owing to the lower symmetry of **3** and the fact that the excitations are each described by many non-negligible configurations, the assignment of excitations is less reliable than for **2**. Regardless, the excitations with the largest contributions to D arise from sextet and quartet states, which involve transitions from the $\sigma/^{P}$1e orbitals to the ^{N}1e orbitals. Unlike the case for **1** and **2**, where states with the same spin as the ground state determine the overall magnitude of D, here we find that states of different spin contribute significantly to the total value. In fact, when we compare the sum of the contributions, we find that the quartet states account for ~65%, the sextet states ~48%, and the octet states ~−13% of the total ZFS. As in the case of **2**, the D value of **3** is significantly smaller than that of **1** due to the projection

https://dx.doi.org/10.1021/acs.inorgchem.0c02605
Inorg. Chem. 2020, 59, 18141−18155

of single-site anisotropies onto the coupled molecular spin state (*vide infra*).

Influence of the Metal−Metal Bond on Magnetic Properties. In exchange-coupled systems it is common to interpret experimental data in terms of a dimer model that considers the individual spin Hamiltonians at each site, as well as a typically isotropic exchange coupling constant. In this manner, the D values at each site are related to the experimentally observed D value using projection coefficients

$$D_{Tot} = C_A D_A + C_B D_B \quad (6)$$

where D_{Tot} is the observed ZFS of the dimer, D_A/D_B are the local ZFS parameters of the indicated sites, and C_A/C_B are the projection coefficients for the indicated local sites. Given the high symmetry and relative clarity of the computational results of **2**, we have generated a pair of models with a single magnetic ion to investigate the effect of the metal−metal bond on the isolated properties of the two iron sites. These models consist of the same structure used in the SA-CASSCF calculation, but one of the Fe sites is replaced with a diamagnetic analogue. In the first model the formally Fe(II) site is replaced with Zn(II); in the second model the formally Fe(I) site is replaced with Cu(I). The calculated ZFS parameters of these local site models are +13.40 cm^{-1} for the Zn(II)Fe(I) model (S = 3/2) and −23.06 cm^{-1} for the Fe(II)Cu(I) model (S = 2).

For **2**, the projection coefficients when the total spin is S = 7/2 are $C_{S=2}$ = 2/7 and $C_{S=3/2}$ = 1/7. The combination of these projection coefficients with the calculated ZFS parameters of the local site models predicts that D_{Tot} = −4.67 cm^{-1} in comparison to +3.42 cm^{-1} calculated for the diiron model of **2**. Perhaps unsurprisingly, this result shows that the magnetic properties of this compound are significantly affected by the presence of the metal−metal bond. We can illustrate this in a qualitative manner by examining the *ab initio* ligand-field theory orbital energies resulting from the SA-CASSCF calculations at the local sites (Figure 10). We can then show the changes in orbital ordering expected by the formation of the metal−metal bond. We have assigned the metal−metal-bonded orbital to each site on the basis of the predominant character of the orbital in the ground state (Figure S7). Using this admittedly oversimplified approach, we determined that the tris(amide) site (FeCu model) has an inverted ordering of the z^2 and xz/yz orbitals. In terms of the ZFS, this inversion will reverse the sign of D from negative to positive. An examination of the tris(phosphine) model (ZnFe) reveals that no change in the ordering of the orbitals occurs and, therefore, we may expect the ZFS to retain its sign. Now that both sites are positive, the spin projection treatment will produce a positive D_{Tot}, as found in both the *ab initio* calculations and experiment. This treatment of course ignores charge transfer contributions to the ZFS but likely captures the main contribution to the origin of the ZFS. In a similar manner, we may compare the calculated isomer shift and quadrupole splitting of our local site models to those calculated for the corresponding truncated diiron model (Table 2). Again, we find that the parameters of the local site models differ substantially from those of the diiron model. Especially striking is the comparison of the parameters of the FeCu model to those of the N site of the diiron model. Here, the quadrupole splitting in the diiron model is reduced to one-third of its magnitude and is of the opposite sign in comparison to the FeCu model. If we assume that the ligand contribution to the EFG is similar in all models, then the difference in sign and magnitude of the EFG can be rationalized by changes to the valence contribution. These observations suggest that the formal oxidation states of the individual sites are not entirely reflective of the sites in the presence of the metal−metal bond and that it is more appropriate to describe this as a single Fe_2 unit with 13 valence electrons.

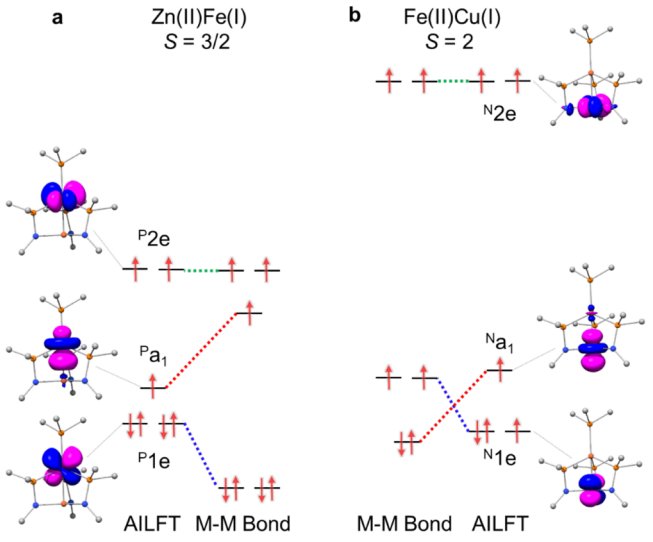

Figure 10. (a) *Ab initio* ligand-field theory (AILFT) derived MO energy level diagram for the Fe(I) local site model (left) in **2**. The hypothetical single-site orbitals after the formation of the metal−metal (M−M) bond are shown to the right. (b) Single-site MO energy level diagram of the Fe(II) local site model (right) in **2**. The hypothetical single-site orbitals after the formation of the metal−metal bond are shown to the left. Note that the orbital ordering of the a_1 and 1e orbitals is inverted by the formation of the metal−metal bond.

Table 2. Calculated Spin Hamiltonian Parameters for Truncated and Single Fe Models of 2[a]

	ox.[b]	S	δ[c] (mm/s)	ΔE_Q[c] (mm/s)	D[d] (cm^{-1})
^{P}**2**	I‡	7/2	0.38	−0.90	+3.42
^{N}**2**	II‡	7/2	0.39	1.08	
ZnFe	I	3/2	0.36	−0.25	+13.40
FeCu	II	2	0.67	−3.12	−23.06

[a]We chose to use the truncated model for this section to be consistent with the geometry used in the CASSCF calculations. The δ and ΔE_Q values are similar for each geometry. [b]Oxidation state for the Fe site or expected oxidation state absent the metal−metal bond. [c]Calculated with DFT. [d]Calculated with SA-CASSCF/NEVPT2.

CONCLUSIONS AND OUTLOOK

We have successfully combined ^{57}Fe Mössbauer spectroscopy, electron paramagnetic resonance, and quantum chemical calculations to probe the electronic structure of compounds that incorporate diiron bonds. We showed that, even at room temperature, the ground spin state of both compounds is thermally isolated from the excited spin states. Regarding the recent utilization of metal−metal bonding as a functional motif for the design of SMMs,[16] this result serves as proof of principle that multiple metal ions linked by metal−metal bonds may serve as a solution to the problem of low-lying spin states that have plagued SMMs based on polynuclear clusters.[6,60−63] The presence of low-lying spin states limits the temperature at

https://dx.doi.org/10.1021/acs.inorgchem.0c02605
Inorg. Chem. 2020, 59, 18141−18155

which the barrier to relaxation is effective by providing alternative QTM relaxation pathways.

To develop potential design strategies for SMMs based on metal−metal bonds, we will now examine the key variables that govern the size of the contributions to ZFS, as shown in eq 4. Perhaps the most obvious (and most discouraging) observation is the $1/S^2$ prefactor, which suggests that increasing the spin may not be inherently beneficial to generating a large energy barrier. However, the barrier height itself is proportional to S^2D, meaning that the barrier may be approximately independent of S. In this way the $1/S^2$ prefactor may not be as detrimental as it appears.[64] The next variable in eq 4 is the one-electron spin−orbit coupling parameter, ζ. The ζ value for an atom for a specific oxidation state is essentially fixed, although it might be reduced from the free ion value by the ligand field. In general, ζ increases as the atomic mass increases and as the oxidation state increases.[65] In this way, there is some room for chemical tailoring of this variable. A tempting strategy may be to employ heavier atoms in the metal−metal bond to exploit their inherently larger ζ value. However, as the atomic number increases, a few other problems arise. For heavier d-block elements (4d/5d) the larger radial extent of the d orbitals induces stronger bonding interactions that tend to favor low-spin states (often with $S = 0$ or $1/2$) and are, therefore, not generally suitable for the design of SMMs.[17,25,66−68] In the case of f-block elements, the decreased radial extension of the f orbitals hinders the formation of metal−metal bonds in most cases. While the 5f orbitals are more diffuse and allow for marginally more covalent interactions in comparison to the isoelectronic lanthanide, it may be more beneficial to exploit the unique redox properties of the actinide elements to engender stronger metal−metal interactions using high-valent actinides.[69,70] However, the limited access and significant hazards involved in working with actinides heavier than uranium limit the utility of actinides for developing molecular materials. Given these considerations, it may be beneficial to utilize 3d elements over their heavier counterparts. An additional strategy, which has been used to great success in developing highly anisotropic monometallic SMMs, requires the stabilization of a degenerate pair of orbitals.[71−73] This involves the nature of the new orbitals formed by the metal−metal bond. As shown above, the metal−metal bond can reorganize the orbital ordering expected for the mononuclear sites. Additionally, a second, subtler effect involves the redistribution of electron density induced by the formation of the new molecular orbitals. By redistribution of the electron density, a covalent reduction to the spin−orbit coupling constant can occur. In the case where the new molecular orbitals are composed of large contributions from each site, the magnitude of the spin−orbit interaction decreases for each site in eq 4. A counterargument to this point may be that exchange matrix elements, i.e., those of the type $\langle \Psi_{\text{Site1}} | \hat{l}_{\text{site1,site2}} | \Psi_{\text{site2}} \rangle$ that couple the orbital on one metal site with an orbital of appropriate symmetry on the other metal site, may make up for this reduction. The competition between these two effects may merit future studies. However, regardless of these effects, the problem may be avoided by designing molecules where the orbitally degenerate pair exists in a set of nonbonding orbitals. In this way, the covalent reduction to the spin−orbit contribution is minimized. By designing orbitally degenerate systems with metal−metal bonds, it may be possible to create a new method for developing SMMs with high blocking temperatures. This will be achieved by the increased isolation of the spin ground state in metal−metal-bonded systems that will suppress higher-order interactions that create pathways for QTM. Thus, the possibility of combining isolated spin states that hamper QTM and high anisotropy should make metal−metal-bonded systems an attractive avenue for the future development of SMMs.

■ ASSOCIATED CONTENT

Supporting Information

The Supporting Information is available free of charge at https://pubs.acs.org/doi/10.1021/acs.inorgchem.0c02605.

Additional experimental and theoretical data including Mössbauer spectra, multifrequency EPR, quantum chemical calculations, and input files (PDF)

■ AUTHOR INFORMATION

Corresponding Authors

Christine M. Thomas − *Department of Chemistry and Biochemistry, The Ohio State University, Columbus, Ohio 43210, United States;* orcid.org/0000-0001-5009-0479; Email: thomasc@chemistry.ohio-state.edu

Sebastian A. Stoian − *Department of Chemistry, University of Idaho, Moscow, Idaho 83844, United States;* orcid.org/0000-0003-3362-7697; Email: sstoian@uidaho.edu

Stephen Hill − *National High Magnetic Field Laboratory and Department of Physics, Florida State University, Tallahassee, Florida 32310, United States;* orcid.org/0000-0001-6742-3620; Email: shill@magnet.fsu.edu

Authors

Samuel M. Greer − *National High Magnetic Field Laboratory and Department of Chemistry and Biochemistry, Florida State University, Tallahassee, Florida 32310, United States;* orcid.org/0000-0001-8225-3252

Kathryn M. Gramigna − *Department of Chemistry, Brandeis University, Waltham, Massachusetts 02453, United States*

Complete contact information is available at: https://pubs.acs.org/10.1021/acs.inorgchem.0c02605

Notes

The authors declare no competing financial interest.

■ ACKNOWLEDGMENTS

A portion of this work was performed at the National High Magnetic Field Laboratory (NHMFL), which is supported by the NSF (DMR-1644779) and the State of Florida. This work used the High Performance Computing Center at Florida State University. The Mössbauer instrument was purchased through the NHMFL User Collaboration Grant Program (UCGP5064) awarded to Dr. Andrzej Ozarowski. S.M.G. acknowledges support from the NSF Graduate Research Fellowship Program (DGE-1449440). Support from the NSF (Grant DMR-1610226 to S.H.) and the U.S. Department of Energy, Office of Science, Office of Basic Energy Sciences, Catalysis Science Program (DE-SC0019179 awarded to C.M.T.) is also acknowledged. S.A.S. acknowledges the support of the University of Idaho.

■ REFERENCES

(1) Reis, M. Molecular Magnetism. In *Fundamentals of Magnetism*; VCH: 2013; pp 193−224. DOI: 10.1016/b978-0-12-405545-2.00012-6.

(2) Gatteschi, D.; Sessoli, R.; Villain, J. *Molecular Nanomagnets*; OUP Oxford: Oxford, 2007. DOI: 10.1093/acprof:oso/9780198567530.001.0001.
(3) Weighardt, K.; Pohl, K.; Jibril, I.; Huttner, G. Hydrolysis Products of the Monomeric Amine Complex $(C_6H_{15}N_3)FeCl_3$: The Structure of the Octameric Iron(III) Cation of $\{[(C_6H_{15}N_3)_6Fe_8(\mu_3\text{-}O)_2(\mu_2\text{-}OH)_{12}]Br_7(H_2O)\}Br{\cdot}8H_2O$. *Angew. Chem., Int. Ed. Engl.* **1984**, *23* (1), 77−78.
(4) Eilers, G. Origin of Satellite Structures of High Field EPR in $Cd_{1\text{-}X}Mn_xTe$. *Chem. Commun.* **2017**, 318.
(5) Sessoli, R.; Gatteschi, D.; Caneschi, A.; Novak, M. A. Magnetic Bistability in a Metal-Ion Cluster. *Nature* **1993**, *365* (6442), 141−143.
(6) Zipse, D.; Dalal, N. S.; Achey, R. M.; North, J. M.; Hill, S.; Edwards, R. S. EPR and NMR Characterization of the S = 9 Excited State and Spin Density Distribution in the Single-Molecule Magnet Fe_8Br_8: Implications to the S = 10 Model and Magnetization Tunneling Pathways. *Appl. Magn. Reson.* **2004**, *27*, 151−163.
(7) Zipse, D.; North, M.; Dalal, S.; Hill, S.; Edwards, S. Characterization of the S = 9 Excited State in Fe8Br8 by Electron Paramagnetic Resonance. *Phys. Rev. B: Condens. Matter Mater. Phys.* **2003**, *68* (18), 184408.
(8) Feng, P. L.; Koo, C.; Henderson, J. J.; Manning, P.; Nakano, M.; del Barco, E.; Hill, S.; Hendrickson, D. N. Nanomodulation of Molecular Nanomagnets. *Inorg. Chem.* **2009**, *48* (8), 3480−3492.
(9) Petukhov, K.; Hill, S.; Chakov, N. E.; Abboud, K. A.; Christou, G. Evidence for the S = 9 Excited State in Mn_{12}-Bromoacetate Measured by Electron Paramagnetic Resonance. *Phys. Rev. B: Condens. Matter Mater. Phys.* **2004**, *70* (5), 054426.
(10) Wilson, A.; Lawrence, J.; Yang, E. C.; Nakano, M.; Hendrickson, D. N.; Hill, S. Magnetization Tunneling in High-Symmetry Single-Molecule Magnets: Limitations of the Giant Spin Approximation. *Phys. Rev. B: Condens. Matter Mater. Phys.* **2006**, *74* (14), 140403.
(11) Hill, S.; Datta, S.; Liu, J.; Inglis, R.; Milios, C. J.; Feng, P. L.; Henderson, J. J.; Del Barco, E.; Brechin, E. K.; Hendrickson, D. N. Magnetic Quantum Tunneling: Insights from Simple Molecule-Based Magnets. *Dalton Trans.* **2010**, *39* (20), 4693−4707.
(12) Lampropoulos, C.; Hill, S.; Christou, G. A Caveat for Single-Molecule Magnetism : Non-Linear Arrhenius Plots. *ChemPhysChem* **2009**, *10*, 2397−2400.
(13) Liu, J.; Del Barco, E.; Hill, S. Quantum Tunneling of Magnetization in Trigonal Single-Molecule Magnets. *Phys. Rev. B: Condens. Matter Mater. Phys.* **2012**, *85* (1), 012406.
(14) Henderson, J. J.; Koo, C.; Feng, P. L.; Del Barco, E.; Hill, S.; Tupitsyn, I. S.; Stamp, P. C. E.; Hendrickson, D. N. Manifestation of Spin Selection Rules on the Quantum Tunneling of Magnetization in a Single-Molecule Magnet. *Phys. Rev. Lett.* **2009**, *103* (1), 017202.
(15) Marbey, J.; Gan, P. R.; Yang, E. C.; Hill, S. Magic-Angle Effects in a Trigonal Mn_3^{III} Cluster: Deconstruction of a Single-Molecule Magnet. *Phys. Rev. B: Condens. Matter Mater. Phys.* **2018**, *98* (14), 144433.
(16) Hernández Sánchez, R.; Betley, T. A. Meta-Atom Behavior in Clusters Revealing Large Spin Ground States. *J. Am. Chem. Soc.* **2015**, *137* (43), 13949−13956.
(17) Hay, P. J.; Thibeault, J. C.; Hoffmann, R. Orbital Interactions in Metal Dimer Complexes. *J. Am. Chem. Soc.* **1975**, *97* (17), 4884−4899.
(18) Pap, J. S.; DeBeer George, S.; Berry, J. F. Delocalized Metal-Metal and Metal-Ligand Multiple Bonding in a Linear Ru-Ru≡N Unit: Elongation of a Traditionally Short Ru≡N Bond. *Angew. Chemie - Int. Ed.* **2008**, *47* (52), 10102−10105.
(19) Kuppuswamy, S.; Powers, T. M.; Johnson, B. M.; Bezpalko, M. W.; Brozek, C. K.; Foxman, B. M.; Berben, L. A.; Thomas, C. M. Metal−Metal Interactions in C_3 -Symmetric Diiron Imido Complexes Linked by Phosphinoamide Ligands. *Inorg. Chem.* **2013**, *52* (9), 4802−4811.
(20) Miller, D. L.; Siedschlag, R. B.; Clouston, L. J.; Young, V. G.; Chen, Y.-S. S.; Bill, E.; Gagliardi, L.; Lu, C. C. Redox Pairs of Diiron and Iron-Cobalt Complexes with High-Spin Ground States. *Inorg. Chem.* **2016**, *55* (19), 9725−9735.
(21) Murillo, C. A. An Iron Complex with an Unsupported Fe-Fe Bond. *Angew. Chem., Int. Ed.* **2009**, *48* (28), 5076−5077.
(22) Hernández Sánchez, R.; Bartholomew, A. K.; Powers, T. M.; Ménard, G.; Betley, T. A. Maximizing Electron Exchange in a $[Fe_3]$ Cluster. *J. Am. Chem. Soc.* **2016**, *138* (7), 2235−2243.
(23) Zall, C. M.; Clouston, L. J.; Young, V. G.; Ding, K.; Kim, H. J.; Zherebetskyy, D.; Chen, Y. S.; Bill, E.; Gagliardi, L.; Lu, C. C. Mixed-Valent Dicobalt and Iron-Cobalt Complexes with High-Spin Configurations and Short Metal-Metal Bonds. *Inorg. Chem.* **2013**, *52* (16), 9216−9228.
(24) Cotton, F. A.; Feng, X.; Murillo, C. A. Electronic Structure of Dinuclear Trigonal-Lantern Amidinato Compounds of Iron and Cobalt. *Inorg. Chim. Acta* **1997**, *256* (2), 303−308.
(25) Krogman, J. P.; Thomas, C. M. Metal-Metal Multiple Bonding in C_3-Symmetric Bimetallic Complexes of the First Row Transition Metals. *Chem. Commun.* **2014**, *50* (40), 5115−5127.
(26) Kuppuswamy, S.; Cooper, B. G.; Bezpalko, M. W.; Foxman, B. M.; Powers, T. M.; Thomas, C. M. Synthesis and Structural Characterization of High Spin M/Cu (M = Mn, Fe) Heterobimetallic and Fe/Cu_2 Trimetallic Phosphinoamides. *Inorg. Chem.* **2012**, *51* (3), 1866−1873.
(27) *WMOSS4, Mössbauer Spectral Analysis Software*. See Co., formerly Web Research Co. Edina, MN.
(28) Hassan, A. K.; Pardi, L. A.; Krzystek, J.; Sienkiewicz, A.; Goy, P.; Rohrer, M.; Brunel, L. C. Ultrawide Band Multifrequency High-Field EMR Technique: A Methodology for Increasing Spectroscopic Information. *J. Magn. Reson.* **2000**, *142* (2), 300−312.
(29) Stoll, S.; Schweiger, A. EasySpin, a Comprehensive Software Package for Spectral Simulation and Analysis in EPR. *J. Magn. Reson.* **2006**, *178* (1), 42−55.
(30) Perdew, J. P. Density-Functional Approximation for the Correlation Energy of the Inhomogeneous Electron Gas. *Phys. Rev. B: Condens. Matter Mater. Phys.* **1986**, *33* (12), 8822−8824.
(31) Becke, A. D. Density-Functional Exchange-Energy Approximation with Correct Asymptotic Behavior. *Phys. Rev. A: At., Mol., Opt. Phys.* **1988**, *38* (6), 3098−3100.
(32) Weigend, F.; Ahlrichs, R. Balanced Basis Sets of Split Valence, Triple Zeta Valence and Quadruple Zeta Valence Quality for H to Rn: Design and Assessment of Accuracy. *Phys. Chem. Chem. Phys.* **2005**, *7* (18), 3297−3305.
(33) Stoychev, G. L.; Auer, A. A.; Neese, F. Automatic Generation of Auxiliary Basis Sets. *J. Chem. Theory Comput.* **2017**, *13* (2), 554−562.
(34) Römelt, M.; Ye, S.; Neese, F. Calibration of Modern Density Functional Theory Methods for the Prediction Of ^{57}Fe Mössbauer Isomer Shifts: Meta-GGA and Double-Hybrid Functionals. *Inorg. Chem.* **2009**, *48* (3), 784−785.
(35) Gorelsky, S. I. Complexes with a Single Metal-Metal Bond as a Sensitive Probe of Quality of Exchange-Correlation Functionals. *J. Chem. Theory Comput.* **2012**, *8* (3), 908−914.
(36) Greer, S. M.; McKay, J.; Gramigna, K. M.; Thomas, C. M.; Stoian, S. A.; Hill, S. Probing Fe-V Bonding in a C_3 -Symmetric Heterobimetallic Complex. *Inorg. Chem.* **2018**, *57* (10), 5870−5878.
(37) Ganyushin, D.; Neese, F. A Fully Variational Spin-Orbit Coupled Complete Active Space Self-Consistent Field Approach: Application to Electron Paramagnetic Resonance g-Tensors. *J. Chem. Phys.* **2013**, *138* (10), 104113.
(38) Andersson, K.; Malmqvist, P. Å.; Roos, B. O.; Sadlej, A. J.; Wolinski, K. Second-Order Perturbation Theory with a CASSCF Reference Function. *J. Phys. Chem.* **1990**, *94* (14), 5483−5488.
(39) Andersson, K.; Malmqvist, P. Å.; Roos, B. O. Second-Order Perturbation Theory with a Complete Active Space Self-Consistent Field Reference Function. *J. Chem. Phys.* **1992**, *96* (2), 1218−1226.
(40) Malmqvist, P. Å.; Roos, B. O. The CASSCF State Interaction Method. *Chem. Phys. Lett.* **1989**, *155* (2), 189−194.
(41) Hess, B. A. Relativistic Electronic-Structure Calculations Employing a Two-Component No-Pair Formalism with External-

https://dx.doi.org/10.1021/acs.inorgchem.0c02605
Inorg. Chem. 2020, 59, 18141−18155

Field Projection Operators. *Phys. Rev. A: At., Mol., Opt. Phys.* **1986**, *33* (6), 3742−3748.
(42) Angeli, C.; Cimiraglia, R.; Malrieu, J. P. N-Electron Valence State Perturbation Theory: A Fast Implementation of the Strongly Contracted Variant. *Chem. Phys. Lett.* **2001**, *350* (3−4), 297−305.
(43) Angeli, C.; Bories, B.; Cavallini, A.; Cimiraglia, R. Third-Order Multireference Perturbation Theory: The n-Electron Valence State Perturbation-Theory Approach. *J. Chem. Phys.* **2006**, *124* (5), 054108.
(44) Angeli, C.; Cimiraglia, R.; Malrieu, J. P. N-Electron Valence State Perturbation Theory: A Spinless Formulation and an Efficient Implementation of the Strongly Contracted and of the Partially Contracted Variants. *J. Chem. Phys.* **2002**, *117* (20), 9138−9153.
(45) Angeli, C.; Cimiraglia, R.; Evangelisti, S.; Leininger, T.; Malrieu, J. P. Introduction of N-Electron Valence States for Multireference Perturbation Theory. *J. Chem. Phys.* **2001**, *114* (23), 10252.
(46) Neese, F. Software Update: The ORCA Program System, Version 4.0. *Wiley Interdiscip. Rev.: Comput. Mol. Sci.* **2018**, *8* (1), e1327.
(47) Nehrkorn, J.; Greer, S. M.; Malbrecht, B.; Aliabadi, A.; Krzystek, J.; Schnegg, A.; Holldack, K.; Herrmann, C.; Betley, T. A.; Stoll, S. Spectroscopic Investigation of a Metal-Metal Bonded Single Molecule Magnet with an Fe_6 Core. Submitted for publication, 2020
(48) Gütlich, P.; Bill, E.; Trautwein, A. X. *Mössbauer Spectroscopy and Transition Metal Chemistry: Fundamentals and Applications*; Springer Berlin Heidelberg: Berlin, Heidelberg, 2011. DOI: 10.1007/978-3-540-88428-6.
(49) Sanakis, Y.; Power, P. P.; Stubna, A.; Münck, E. Mössbauer Study of the Three-Coordinate Planar Fe^{II} Thiolate Complex $[Fe(SR)_3]$- (R = C_6H_2−2,4,6-TBu_3): Model for the Trigonal Iron Sites of the $MoFe_7S_9$:Homocitrate Cofactor of Nitrogenase. *Inorg. Chem.* **2002**, *41* (10), 2690−2696.
(50) Eichhöfer, A.; Lan, Y.; Mereacre, V.; Bodenstein, T.; Weigend, F. Slow Magnetic Relaxation in Trigonal-Planar Mononuclear Fe(II) and Co(II) Bis(Trimethylsilyl)Amido Complexes - A Comparative Study. *Inorg. Chem.* **2014**, *53* (4), 1962−1974.
(51) Zall, C. M.; Zherebetskyy, D.; Dzubak, A. L.; Bill, E.; Gagliardi, L.; Lu, C. C. A Combined Spectroscopic and Computational Study of a High-Spin S = 7/2 Diiron Complex with a Short Iron-Iron Bond. *Inorg. Chem.* **2012**, *51* (1), 728−736.
(52) Zhang, Y.; Oldfield, E. An Investigation of the Unusual ^{57}Fe Mössbauer Quadrupole Splittings and Isomer Shifts in 2 and 3-Coordinate Fe(II) Complexes. *J. Phys. Chem. B* **2003**, *107* (29), 7180−7188.
(53) Stoian, S. A.; Vela, J.; Smith, J. M.; Sadique, A. R.; Holland, P. L.; Münck, E.; Bominaar, E. L. Mössbauer and Computational Study of an N_2-Bridged Diiron Diketiminate Complex: Parallel Alignment of the Iron Spins by Direct Antiferromagnetic Exchange with Activated Dinitrogen. *J. Am. Chem. Soc.* **2006**, *128* (31), 10181−10192.
(54) Bucinsky, L.; Breza, M.; Lee, W. T.; Hickey, A. K.; Dickie, D. A.; Nieto, I.; Degayner, J. A.; Harris, T. D.; Meyer, K.; Krzystek, J.; et al. Spectroscopic and Computational Studies of Spin States of Iron(IV) Nitrido and Imido Complexes. *Inorg. Chem.* **2017**, *56* (8), 4751−4768.
(55) Long, G. J.; Hautot, D.; Mohan, A.; Hughbanks, T.; Xie, X.; Grandjean, F. Compounds with Extremely Negative Mossbauer-Effect Isomer Shifts: A Probe of Intermetallic Bonding in $Zr_6Cl_{14}Fe$, $LiZr_6Cl_{15}Fe$, and $KZr_6Cl_{15}Fe$. *J. Am. Chem. Soc.* **1998**, *120*, 12163−12164.
(56) Abouelwafa, A. S.; Hauser, A.; Mereacre, V.; Lan, Y.; Long, G. J.; Grandjean, F.; Buth, G.; Anson, C. E.; Powell, A. K. Search for Electron Delocalization from $[Fe(CN)_6]^{3-}$ to the Dication of Viologen in $(DNP)_3[Fe(CN)_6]2.10H_2O$. *Inorg. Chem.* **2017**, *56* (11), 6477−6488.
(57) Hendrich, M. P.; Gunderson, W.; Behan, R. K.; Green, M. T.; Mehn, M. P.; Betley, T. A.; Lu, C. C.; Peters, J. C. On the Feasibility of N_2 Fixation via a Single-Site Fe^I/Fe^{IV} Cycle: Spectroscopic Studies of $Fe^I(N_2)Fe^I$, $Fe^{IV}{\equiv}N$, and Related Species. *Proc. Natl. Acad. Sci. U. S. A.* **2006**, *103* (46), 17107−17112.
(58) Neese, F.; Solomon, E. I. Calculation of Zero-Field Splittings, g-Values, and the Relativistic Nephelauxetic Effect in Transition Metal Complexes. Application to High-Spin Ferric Complexes. *Inorg. Chem.* **1998**, *37* (26), 6568−6582.
(59) Atanasov, M.; Aravena, D.; Suturina, E.; Bill, E.; Maganas, D.; Neese, F. First Principles Approach to the Electronic Structure, Magnetic Anisotropy and Spin Relaxation in Mononuclear 3d-Transition Metal Single Molecule Magnets. *Coord. Chem. Rev.* **2015**, *289−290* (1), 177−214.
(60) Lawrence, J.; Yang, E. C.; Hendrickson, D. N.; Hill, S. Magnetic Quantum Tunneling: Key Insights from Multi-Dimensional High-Field EPR. *Phys. Chem. Chem. Phys.* **2009**, *11* (31), 6743−6749.
(61) Hill, S.; Datta, S.; Liu, J.; Inglis, R.; Milios, C. J.; Feng, P. L.; Henderson, J. J.; Del Barco, E.; Brechin, E. K.; Hendrickson, D. N. Magnetic Quantum Tunneling: Insights from Simple Molecule-Based Magnets. *Dalton Trans.* **2010**, *39* (20), 4693−4707.
(62) Krzystek, J.; Ozarowski, A.; Telser, J. Multi-Frequency, High-Field EPR as a Powerful Tool to Accurately Determine Zero-Field Splitting in High-Spin Transition Metal Coordination Complexes. *Coord. Chem. Rev.* **2006**, *250* (17−18), 2308−2324.
(63) Katsnelson, M. I.; Dobrovitski, V. V.; Harmon, B. N. Many-Spin Model and the Spin Hamiltonian of Mn_{12} Clusters. *J. Appl. Phys.* **1999**, *85*, 4533−4535.
(64) Neese, F.; Pantazis, D. A. What Is Not Required to Make a Single Molecule Magnet. *Faraday Discussions* **2011**, 229−238.
(65) Bendix, J.; Brorson, M.; Schaffer, C. E. Accurate Empirical Spin-Orbit Coupling Parameters ζ_{nd} for Gaseous nd^q Transition Metal Ions. The Parametrical Multiplet Term Model. *Inorg. Chem.* **1993**, *32*, 2838−2849.
(66) Dalal, N. S.; Murillo, C. A. The Usefulness of EPR Spectroscopy in the Study of Compounds with Metal-Metal Multiple Bonds. *Dalton Trans.* **2014**, *43* (23), 8565−8576.
(67) Liddle, S. T. In *Molecular Metal-Metal Bonds: Compounds, Synthesis, Properties*; Liddle, S. T., Ed.; Wiley-VCH: Weinheim, Germany, 2015. DOI: 10.1002/9783527673353.
(68) Cotton, F. A. Metal-Metal Bonding in $[Re_2X_8]^{2-}$ Ions and Other Metal Atom Clusters. *Inorg. Chem.* **1965**, *4* (3), 334−336.
(69) Morss, L. R.; Edelstein, N. M.; Fuger, J.; Katz, J. J.; Joseph, J. *The Chemistry of the Actinide and Transactinide Elements*; Springer: 2008. DOI: 10.5860/choice.44-4454.
(70) Rinehart, J. D.; Harris, T. D.; Kozimor, S. A.; Bartlett, B. M.; Long, J. R. Magnetic Exchange Coupling in Actinide-Containing Molecules. *Inorg. Chem.* **2009**, *48* (8), 3382−3395.
(71) Marriott, K. E. R.; Bhaskaran, L.; Wilson, C.; Medarde, M.; Ochsenbein, S. T.; Hill, S.; Murrie, M. Pushing the Limits of Magnetic Anisotropy in Trigonal Bipyramidal Ni(II). *Chem. Sci.* **2015**, *6* (12), 6823−6828.
(72) Atanasov, M.; Zadrozny, J. M.; Long, J. R.; Neese, F. A Theoretical Analysis of Chemical Bonding, Vibronic Coupling, and Magnetic Anisotropy in Linear Iron(II) Complexes with Single-Molecule Magnet Behavior. *Chem. Sci.* **2013**, *4* (1), 139−156.
(73) Palii, A. V.; Clemente-Juan, J. M.; Coronado, E.; Klokishner, S. I.; Ostrovsky, S. M.; Reu, O. S. Role of Orbital Degeneracy in the Single Molecule Magnet Behavior of a Mononuclear High-Spin Fe(II) Complex. *Inorg. Chem.* **2010**, *49* (17), 8073−8077.

https://dx.doi.org/10.1021/acs.inorgchem.0c02605
Inorg. Chem. 2020, 59, 18141−18155